Journal of Water Process Engineering 44 (2021) 102376

Contents lists available at ScienceDirect

Journal of Water Process Engineering

journal homepage: www.elsevier.com/locate/jwpe

Photocatalytic and toxicity evaluation of local dyeing wastewater by aluminium/boron doped WO_3 nanoparticles

J.O. Tijani [a,c], M.N. Abdullahi [a,c], M.T. Bankole [a,c], S. Mustapha [a,c,*], T.C. Egbosiuba [b], M. M. Ndamitso [a,c], A.S. Abdulkareem [b,c,d], E. Muzenda [d]

[a] Department of Chemistry, Federal University of Technology, PMB 65, Minna, Niger State, Nigeria
[b] Department of Chemical Engineering, Federal University of Technology, PMB 65, Minna, Niger State, Nigeria
[c] Nanotechnology Research Group, Centre for Genetic Engineering and Biotechnology (CGEB), Federal University of Technology, PMB 65, Bosso, Minna, Niger State, Nigeria
[d] Department of Chemical, Material and Metallurgical Engineering, Botswana International University of Science and Technology, Botswana

ARTICLE INFO

Keywords:
Nanoparticles
Wet impregnation
Surface area
Photocatalytic activity
Local dyeing wastewater

ABSTRACT

The photocatalytic degradation of local dyeing wastewater by Al/B co-doped WO_3 nanoparticles under natural sunlight was investigated. Al/B doped WO_3 nanoparticles were prepared by wet impregnation method and characterized by different analytical tools. *Daphnia magna* was utilized to evaluate the acute toxicity of the untreated and treated wastewater. HRSEM/HRTEM analysis confirmed the formation of agglomerated spherical shape for WO_3 nanoparticles and mixture of spherical and rod-like morphology for Al/B doped WO_3 nanocomposites. XRD analysis demonstrated the formation of monoclinic phase and the addition of Al and B did not change the phase of WO_3 nanoparticles. The BET surface area of Al/B/WO_3 nanocomposites (66.94 m^2/g) is higher than undoped WO_3 (22.49 m^2/g). The XPS analysis suggested substitutional replacement of oxygen either by the dopants and existence of W in +6 oxidation state. Bandgap energy reduced from 2.42 eV to 1.70 eV due to the immobilization of Al and B. The Al/B immobilized WO_3 nanoparticles exhibited enhanced photocatalytic performance with 94.0% and 90.0% reduction of COD and TOC level. The concentration of Zn, Fe, Ni, Cu, Cr and Pb in dyeing wastewater reduced after treatment. The kinetic data showed that the photodegradation of the dyeing wastewater by Al/B doped WO_3 nanocomposites was faster than WO_3 alone and the experimental kinetic data were best suitable for pseudo-first order model. The treated wastewater had little or almost no toxicity after 24 h and the photocatalyst can be reused for 5 cycles. Due to its excellent photocatalytic capacity, Al/B co-doped WO_3 nanoparticles exhibited a significant enhancement in the degradation of local dyeing wastewater.

1. Introduction

In developing countries, small-scale industry like local dyeing operation (dye and tie) has been identified as one of the major consumers of fresh water, dyes and chemicals during their operations [1]. The activities of this cottage industries resulted to indiscriminately release of large quantities of untreated wastewater containing organic dyes, pigments, biocides, surfactants and several other organic and inorganic compounds into the environment causing diverse adverse effects on plants and animals [2,3]. Local dyeing wastewaters contain acids, surfactants, dispersants which are responsible for high biochemical oxygen demand (BOD), chemical oxygen demand (COD), total organic carbon (TOC), pH, total dissolved solids (TDS), colour, turbidity, oil and grease, anions and heavy metals such as chromium, copper and cadmium amongst others [4]. Organic dyes remain integral component of local dyeing wastewater and are main contaminators of water resources [2,5]. Thus, based on the complexity and variability of the local dyeing wastewater, there is need for the reduction of priority substances to recommend limits prior to discharge to the environment.

Several conventional methods such as coagulation-flocculation, sedimentation [6], precipitation and co-precipitation [7], ozonation, ion-exchange and membrane filtration [8], activated carbon adsorption, electro-coagulation [9], amongst others have been used for the treatment of wastewater. Some of these methods are relatively slow, highly expensive; generate toxic sludge which occupies space and low efficiencies and cannot completely remove the contaminants [10]. These

* Corresponding author at: Department of Chemistry, Federal University of Technology, PMB 65, Minna, Niger State, Nigeria.
E-mail address: saheedmustapha09@gmail.com (S. Mustapha).

https://doi.org/10.1016/j.jwpe.2021.102376
Received 4 July 2021; Received in revised form 5 October 2021; Accepted 9 October 2021

often in most cases resulted to additional disposal and extra cost. In addition, physicochemical parameters analysis of wastewater vis-a-viz colour reduction is no longer acceptable nowadays to establish the impact of pollution/pollutants on aquatic species [11]. Different tests such as bioluminescence tests with *Vibrio fischeri* and growth; inhibition tests with *Pseudomonas putida*, the acute *Daphnia magna* and algae growth inhibition tests have been used to evaluate the toxicity of wastewater [12]. Studies have established the toxic effects of raw and treated dyeing wastewater to *D. magna* and found to be less toxic [13]. In this study, acute toxicity test of *D. magna* is employed for monitoring of wastewater due to its sensitivity to different kind of pollutants.

Furthermore, researchers have applied heterogeneous semiconductor metal oxides such as WO_3 nanomaterial for destruction of microbes and harmful pollutants in wastewater due to its low cost, availability, environmental friendliness, biological and chemical stability [14–15]. The photocatalytic activity is based on the absorption of photon either solar, UV or visible light by WO_3 which cause electrons transferred from valence band (VB) to conduction band (CB) and generate electron-hole pairs and through the migrations; oxidation or reduction reactions. These usually occurred on the surface of the metal oxides and eventually lead to production of hydroxyl and superoxide radicals [16]. These free reactive radicals then attack the organic pollutants in wastewater and break it into compounds such as CO_2 and H_2O. WO_3 is an n-type semiconductor with moderate band gap (~2.7–2.8 eV), has exceptional physical and chemical properties such as high electric resistivity, low surface area and high oxidation power which enable its potential applications [17–18]. WO_3 exists in different polymorphs namely hexagonal, orthorhombic and monoclinic and nanostructural network (nanoparticles, nanoplatelets, nanorods, and nanowires) [19–20] with monoclinic phase found to be more photocatalytically active under UV light than hexagonal or orthorhombic phase [21]. However, utilization of UV light is not economically feasible and a viable option for the treatment of large amounts of industrial wastewater. In view of this, development of natural sunlight active catalyst has been identified as a green technology for water and wastewater treatment across the globe because sunlight is readily available, cheap, abundant, environmental friendly and renewable.

More so, the optical response and catalytic activity of WO_3 can be tailored to the visible region via doping with metals, non-metals, metal oxides, and metalloids, encapsulation, functionalization, and coupling with another semiconductor or compositing with other materials [17,22]. Doping is one of the strategies often employ to induce visible light activity by altering the band gap of the WO_3 nanoparticles and prevent electron-hole recombination rates and by extension, improve the photocatalytic performance in the visible region [23]. The additions of the metals such as Pt, Au and Ag to WO_3 material have been reported to enhance photocatalytic activity in the visible than ordinary WO_3. However, metal doping cause reduction of photocatalytic activity and thermal instability [23]. On the contrary, doping with non-metals such as S, P, N or C can enhance the surface area and the performance of the WO_3 based photocatalyst [20,24]. More so, introduction of non-metal onto lattice structure of WO_3 usually caused bonding of p states and 2p states of non-metal and oxygen in W. This orbital interaction resulted to upwards shifting in the valence band edge and reduction in the band gap. Recently, immobilization of metal and non-metal, have been predicted as a feasible alternative to modify WO_3 nanostructure for better performance under visible light [25]. In this study, aluminium and boron were selected as co-dopants for the synthesis of WO_3 due to their low toxicity, availability of the material, tendency to replace oxygen and ability to suppress electron-hole recombination rate and by extension lowering the band gap energy of WO_3 [22,26].

Boron has the potential of forming local network structures and surface-active sites for photocatalytic reactions [27]. Thus, it is expected that combination of Al and B material will improve the quantum efficiency and photocatalytic activity of WO_3. WO_3 nanoparticles have been synthesized by various physical and chemical methods such as solvothermal reduction [19], hydrothermal [28], sol-gel [29], non-sputtering and electrochemical technique [29], catalytic chemical vapour deposition, photo reduction and deposition and others [15,30]. However, these methods are costly, generate toxic byproducts and require complex synthetic procedures as well as high pressure and energy [31]. Conversely, green synthesis involving the uses of plant extracts for the preparation of nanoparticles has several advantages such as presence of metabolites when compared to other methods. These phytochemical constituents are responsible for the stabilization, capping and reduction of metals from their respective oxidation state to zero valence state [32]. *Carrica papaya* belongs to family Caricaceae known as Papaya, Paw Paw, Kates and Papaw is rich in vitamins, phenols, proteolytic acts as good antioxidant, reducing and antimicrobial agent. Banala et al. [61] reported the reduction of silver in oxidation state of +1 to silver in zero valent by *C. papaya* aqueous extract.

Several studies have been reported the photocatalytic activity of WO_3 for the degradation of organic pollutants in aqueous solution under simulated and natural sunlight; Rhodamine blue [17]; monuron [33]; Lidocaine [9], Amoxicillin [30]; rhodamine B (rhB), indigo carmine (IC) and Congo red (CR), [34]; and ethylene [35]. Similarly, there have been many reports on the photodegration of organic contaminants in aqueous matrix either by metals doped WO_3, non-metals doped WO_3 or metal oxides coupled WO_3 under different light sources such as Methylene blue, PdO/WO_3 [15]; Methylene blue, P/WO_3 [18], Methylene blue, Pt/WO_3 [36]; 4-nitrophenol, B-WO_3 [22]. Our research group had earlier reported the photocatalytic degradation of local dyeing wastewater by P-I/WO_3 and $Ag_2O/B_2O_3/TiO_2$ nanocomposites [37,38]. However, toxicity test of untreated and treated wastewater was not carried out. The role of Al and B on the morphology, optical, textural and catalytic properties of WO_3 nanoparticles was not examined.

However, no comprehensive report on the potentials of Al/B immobilized WO_3 nanoparticles for the degradation of organic pollutants in local dyeing wastewater under natural sunlight has been reported to date. Herein, the present study report for the first time the preparation of Al/B immobilized WO_3 nanoparticles using green-wet impregnation method. The prepared Al/B/WO_3 nanocomposites were characterized using several analytical techniques. This was followed by the photodegradation of the local dyeing wastewater by the prepared WO_3 nanoparticles and Al/B/WO_3 nanocomposites under natural sunlight irradiation by measuring change in indicator parameters (TOC and COD level) as a function of time. The acute toxicity level of the chemicals presents in the untreated and treated local dyeing effluent was also investigated using *D. magna* as a test organism. The mechanism of degradation of organic compounds in dyeing wastewater by Al/B/WO_3 photocatalyst under natural sunlight irradiation is also proposed. Lastly, the recycleability potentials of Al/B/WO_3 photocatalyst after five repeated cycles were reported and the stability of the nanocatalyst was before and after was examined using XRD and HRSEM.

2. Materials and methods

2.1. Material

The analytical grade chemicals/reagents namely ammonium tungsten hydrate, boric acid, aluminium oxide, sodium hydroxide, trioxonitrate (V) acid with percentage purity in the range of 99.5–99.9% were obtained from Sigma Aldrich and used without further purification. The leaves of *C. papaya* were randomly collected from different locations in Minna metropolis and subsequently transported to the laboratory. The collected *C. papaya* leaves were washed with distilled water to remove dust particles and later air-dried at room temperature for 2 weeks. The dried leaves were cut into pieces, pound in a wooden mortal and sieved through 2 μm sieve to obtain a fine powder and thereafter stored in a dry container ready for analysis. Green synthesis of WO_3 nanoparticles have been reported in our previous study [31]. The local dyeing wastewater used for the experiment was collected from

different pits in Kwali Area Council of Abuja into a clean 50 L plastic container in the month of October 2020. The samples were transported on ice to the laboratory and stored in the fridge at 4 °C for the entire study period.

2.2. Chemical analysis of local dyeing wastewater

The collected dyeing wastewater was characterized for the following parameters: chemical oxygen demand (COD), total organic carbon (TOC), pH, alkalinity, odour, colour and turbidity. COD was measured by a closed reflux colorimetric method while TOC was determined by TOC analyzer (model, Shimazu 5050A) [39]. The pH of the wastewater was determined by pH meter probe, conductivity was measured using a multi-parameter water quality meter while colour was determined using a UV–visible spectrophotometer (model, Shimadzu UV 1800) [40]. The APHA-2130 B (Nephelometric Method) was used to get the turbidity through the reading from Turbidity Meter. For nitrates and sulphate, colorimetric method was used for their determination. The following reagents; NitraVer 5 Nitrate pillow, sulphate reagent pillow for nitrate, and sulphate respectively were added to each sample cell containing some wastewater and mixed. The mixtures were run in the Hach colorimeter, and results were recorded in mg/L. Chloride determination was carried out using Argentometric method. Nitric acid digestion method described by [41] was employed before heavy metal contents analysis. Heavy metal contents (Zn, Fe, Cr, Cd, Pb and Ni were determined by Atomic Absorption Spectroscopy (AAS) (Perkin Elmer 200 Atomic Absorption Spectrophotometer). The determination of each parameter was carried out three times and average values including their standard deviation were recorded [40].

2.3. Synthesis of Al/B/WO_3 nanocomposites

Firstly, the preparation of Al doped-WO_3 nanoparticle was carried out by mixing 10 mL of 0.05 mol L^{-1} aluminium oxide solution drop wise with the prepared WO_3 nanoparticles and stirred continuously on magnetic stirrer at 1000 rpm for 2 h. Subsequently, the mixture was centrifuged at 1000 rpm for 15 min and washed several times with distilled water and further centrifuged at 1000 rpm. The separated sample was oven dried at 80 °C for 3 h and later calcined at 550 °C in a furnace for 2 h [14]. This procedure was repeated using 0.1 mol L^{-1} and 0.2 mol L^{-1} of aluminium oxide as dopant. Secondly, the preparation of B doped-WO_3 nanoparticle was carried out by mixing 10 mL of 0.05 mol L^{-1} boric acid solution drop wise with the prepared WO_3 nanoparticles. The synthesis was carried out following the aforementioned route for Al doped WO_3 [15–16]. Lastly, the preparation of Al/B/WO_3 nanocomposite was carried out by firstly mixed 10 mL of 0.1 mol L^{-1} aluminium oxide with equal volume of 0.1 mol L^{-1} boric acid solution. Thereafter, 2 g of prepared WO_3 nanoparticles were added to the mixture and stirred on a magnetic stirrer at 1000 rpm for 15 min and the residue was washed several times with distilled water and further centrifuged at 1000 rpm for 15 min. The separated samples were then oven dried at 100 °C for 3 h and later calcined in the furnace at 550 °C for 2 h [14].

2.4. Characterization of WO_3 and Al/B/WO_3 nanocomposites

The prepared WO_3 based nanomaterials were characterized using the following analytical instruments; the mineralogical phases were identified using X-ray diffractometer (XRD)-D8 Bruker AXS advance, fitted with Lynxeye detector and CuKα X-ray source. The morphology and elemental composition of the prepared samples were obtained using Zeiss Auriga High Resolution Scanning Electron Microscope (HRSEM) fitted with a secondary electron detector and an Energy Dispersive X-ray spectroscopy (EDS) option. High Resolution Transmission Electron Microscopy model Zeiss Auriga operated at acceleration voltage of 20 kV was used to examine the microstructure and particle size. UV–Visible spectroscopy in this case, the Shimadzu UV 1800 was used to determine the wavelength of absorption. The X-ray photoelectron Spectroscopy surface was used to examine the surface oxidation state of the elements in the samples. The specific surface area of the synthesized undoped and doped WO_3 nanoparticles were determined using a NOVA 2400e by applying N_2 as an adsorbate on a micrometer ASAP 2020 chemisorption surface area analyzer.

2.5. Adsorption, photolysis and photocatalytic studies

Prior to photocatalytic activity experiments, a control (blank) experiment was carried out by exposing local dyeing wastewater alone to sunlight irradiation as well as prepared catalyst alone in the dark without sunlight. For the adsorption experiment, 0.05 g of each prepared catalyst was added to 100 cm^3 of the local dyeing wastewater in a 250 cm^3 conical flask. The flask was corked and stirred on a magnetic stirrer at 200 rpm for 6 h in the dark to allow for sample homogeneity. The solution (20 cm^3) was sampled periodically at regular interval of 1 h and immediately analyzed for COD and TOC. This was done to establish that the percentage degradation or removal of the organic compounds in the wastewater was due to adsorption only. In addition, another control experiment was carried out by exposing 100 cm^3 of the local dyeing wastewater to sunlight irradiation in the absence of the prepared catalyst and stirred with a magnetic stirrer at 200 rpm for 6 h. Again, 20 cm^3 of the solution was periodically sampled at regular interval and analyzed for COD and TOC in order to establish that the percentage degradation of the local dyeing wastewater was via photolysis alone.

The photocatalytic activities of the synthesized catalysts were evaluated via the degradation of organic compounds in local dyeing wastewater under natural sunlight irradiation. For each experiment, 10 mg of the prepared WO_3, Al doped WO_3, B doped WO_3, and Al/B doped WO_3 were added separately into 250 cm^3 beakers each containing 100 cm^3 of local dyeing wastewater. The mixtures were stirred at 200 rpm for 1 h in darkness to allow for adsorption-desorption process prior to exposure to sunlight irradiation. Thereafter, the mixture was exposed to sunlight (252.92 W/m^2) at 36 °C and agitated on a magnetic stirrer for 6 h. A volume of 20 cm^3 of the solutions were sampled simultaneously, at interval of 1 h and immediately analyzed for COD and TOC. This was done to establish whether the degradation of the wastewater was due to photocatalysis.

2.6. Reusability test

The regeneration studies for WO_3, Al/WO_3, B/WO_3 and Al/B/WO_3 were evaluated using 0.1 mol L^{-1} NaOH solution as a desorption medium. By adding 10 mg each of the dyeing water adsorbed nanoparticles to 100 cm^3 of 0.1 mol L^{-1} NaOH, the mixtures were stirred continuously for 30 min at ambient temperature and copiously washed with deionized water to remove the desorbing species. Thereafter, the regenerated WO_3, Al/WO_3, B/WO_3 and Al/B/WO_3 were reutilized for 5 cycles to determine the effectiveness of the nanoparticles.

2.7. Acute toxicity of raw and treated wastewater

D. magna collected from Council for Scientific and Industrial Research (CSIR), Stellenbosch, South Africa were first cultured following Korea standard procedures [1,40]. Cultures were maintained in a growth chamber at 21 ± 1 °C and 16 h light: 8 h dark photoperiod was employed. The media were changed every 2 days, and the daphnids were fed daily with 5 mL yeast:Ceropyll®:Tetramin® and 3 mL living Chlorella. Water qualities of the culture media were maintained as follows: pH, 7.4–7.8; hardness, 80–100 mg L^{-1} as $CaCO_3$; and alkalinity, 57–64 mg L^{-1} as $CaCO_3$. The acute toxicity test was performed as follows: 10 mL of undiluted raw and treated wastewater were measured independently into 6 separate well plates followed by the introduction of 10 active *D. magna* neonates (12 h after birth). Aerated tap water was

used as the control and the experiment was monitored for 48 h of exposure (12 h illumination/d). *Daphnia* species were not fed during the period under investigation. After the exposure period, the number of inhibited *D. magna* in each group was counted and recorded. The acute toxicities unit (TU) expressed as growth inhibition with no response to the movement of water was calculated using Eq. (1)

$$TU = \frac{100}{LC_{50}} \quad (1)$$

where, the values of LC_{50} were estimated at 24 and 48 h using probit analysis and later put into Eq. (1) to obtain TU. The Probit Programme Version 1.5 was used to perform the calculations and the results were obtained at 95% Confidence Limits [12–13].

3. Results and discussion

3.1. Characterization of nanoparticles

3.1.1. HRSEM analysis of undoped and Al doped WO_3 nanoparticle

HRSEM analysis of the synthesized Al doped WO_3 nanoparticles and the micrograph obtained at different concentration of aluminium is shown in Fig. 1(b–d). Unlike the undoped WO_3 nanoparticle with highly dispersed less aggregated, spherical shape (Fig. 1(a)). Plate-like morphologies were noticed when 0.05 mol L^{-1} of aluminium precursor was incorporated onto the lattice layer WO_3 nanoparticles (Fig. 1(d)). When the concentration of aluminium precursor was increased to 0.1 mol L^{-1}, uniformly distributed agglomerated spherical with less ring-like structure were observed. In the case of 0.2 mol L^{-1} Al doped WO_3 nanoparticle, mixture of agglomerated spherical and spheres ring-like shape was observed. The changes in morphology of undoped WO_3 from spherical to mixture of agglomerated spherical and ring-like shape may be due to aluminium doping effect. This can be explained in terms of small ionic radius of Al (0.535 Å) as compared to W (2.02 Å) and O (1.207 Å) which diffused easily into the pores of WO_3 nanoparticles. The Al dopant exhibited adsorption phenomenon onto charge energy distribution tungsten surface which in turn affect the crystal growth and morphological transformation behavior of WO_3 nanoparticles [42]. It should be noted that as the concentration of aluminium precursor increase, the proportions of spherical shapes outweighed the plate-like structures. This means that morphological changes was a function of concentration of aluminium oxide in the matrix of WO_3 nanoparticle. The average particle sizes of 0.05 mol L^{-1}, 0.1 mol L^{-1} and 0.2 mol L^{-1} Al doped WO_3 nanoparticle were in ascending order of 28.3 nm >18.6 nm > 21.1 nm. This indicates that at high concentration of 0.2 mol L^{-1} of aluminium was able to penetrate into the lattice structure of the WO_3 without completely changed the morphology and structure of WO_3 nanoparticle, which agreed with the findings of Prabhu et al. [43].

3.1.2. HRTEM with corresponding SAED of Al doped WO_3 nanoparticles

The HRTEM with micrographs at high and low magnification with their respective SAED images of Al doped WO_3 nanoparticles are presented in Fig. 2.

For 0.05 mol L^{-1} Al doped WO_3 shown in Fig. 2(a) highly agglomerated particles were formed. In contrast, dense spherical and cubic structures were noticed for WO_3 nanoparticles doped with 0.1 and 0.2 mol L^{-1} aluminium precursor. The spherical and cubic morphologies increase with increasing concentration of aluminium precursor. The changes of morphologies from spherical to cubic may be ascribed to the excessive incorporation of Al^{3+} into the host lattice of WO_3. This finding is in agreement with the HRSEM result in Fig. 2(e–g) and the EDS result

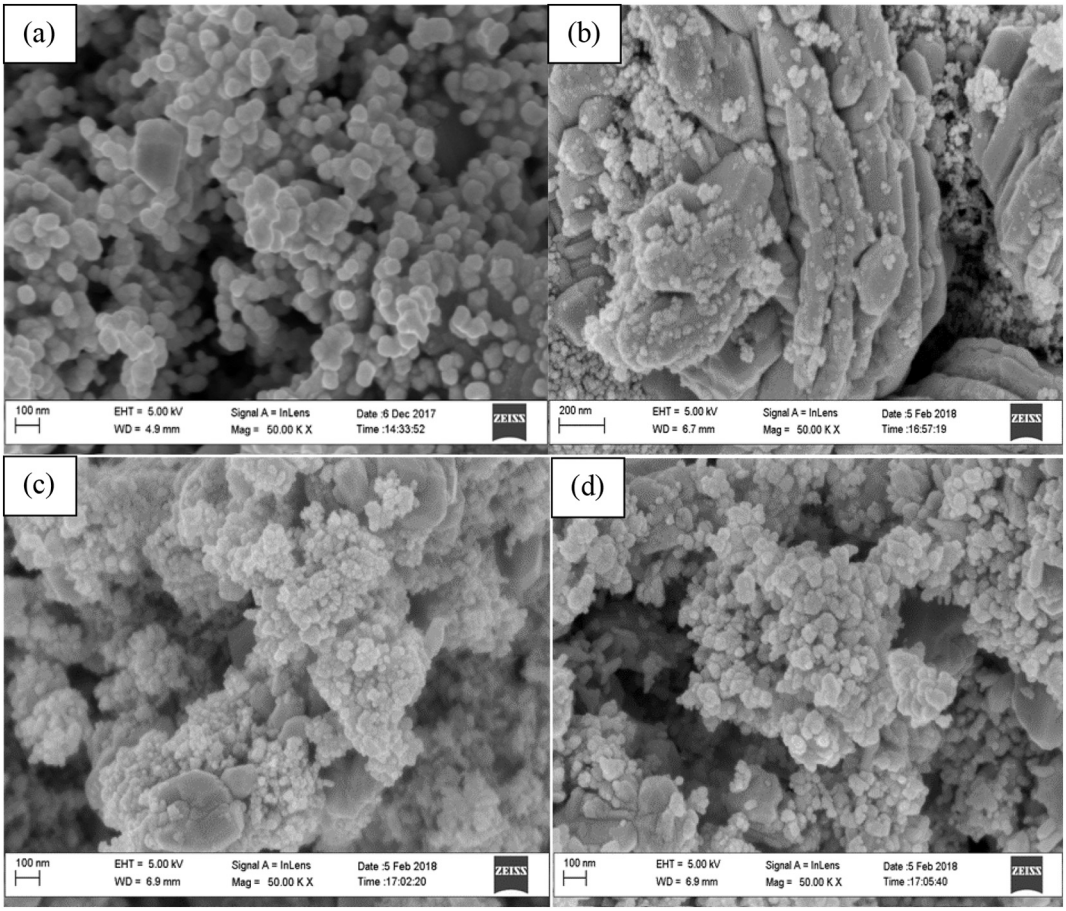

Fig. 1. HRSEM micrograph of (a) undoped WO_3 (b) 0.05 mol L^{-1} (c) 0.1 mol L^{-1} (d) 0.2 mol L^{-1} Al doped WO_3 nanoparticles.

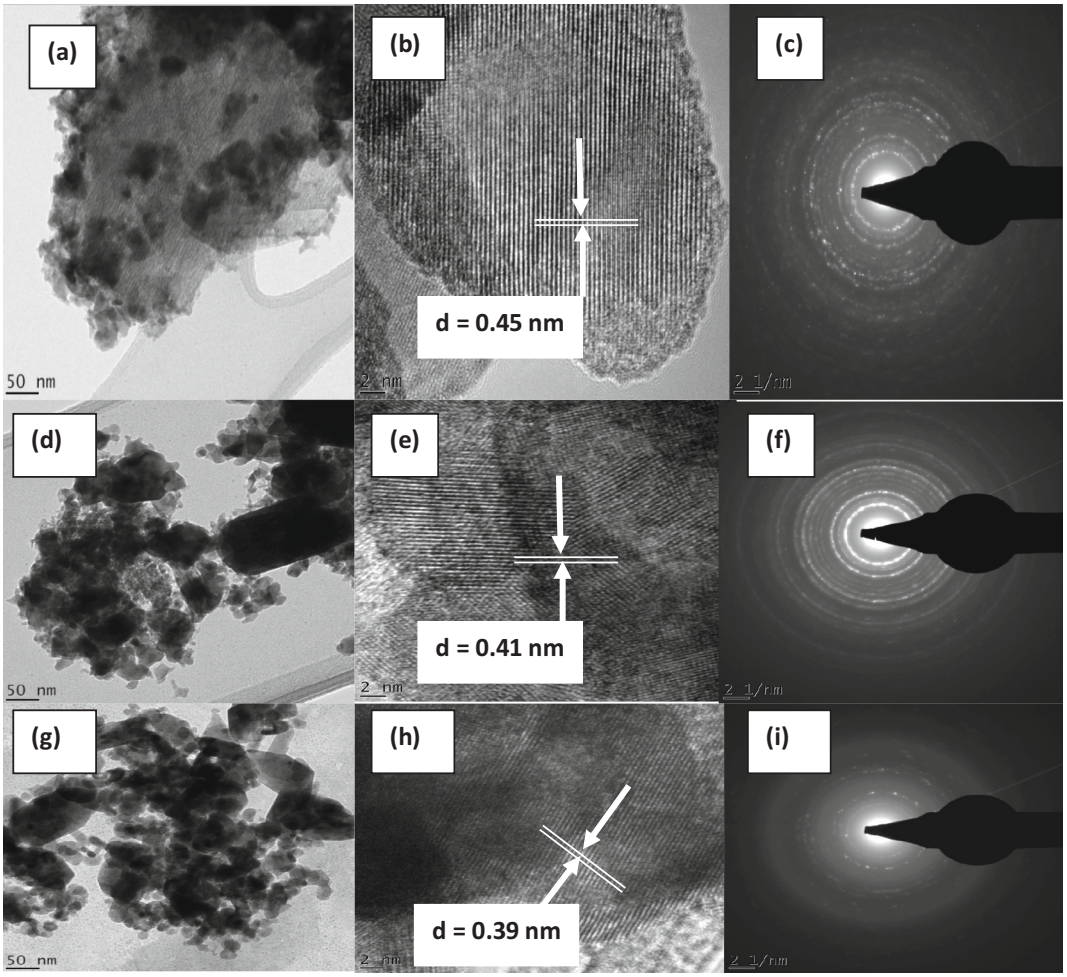

Fig. 2. HRTEM micrograph of WO_3 nanoparticle doped with Al (a) 0.05 mol L^{-1}, (d) 0.1 mol L^{-1} and (g) 0.2 mol L^{-1} at high magnification while (b) 0.05 mol L^{-1}, (e) 0.1 mol L^{-1} and (h) 0.2 mol L^{-1} Al doped WO_3 at low magnification with their corresponding SAED images.

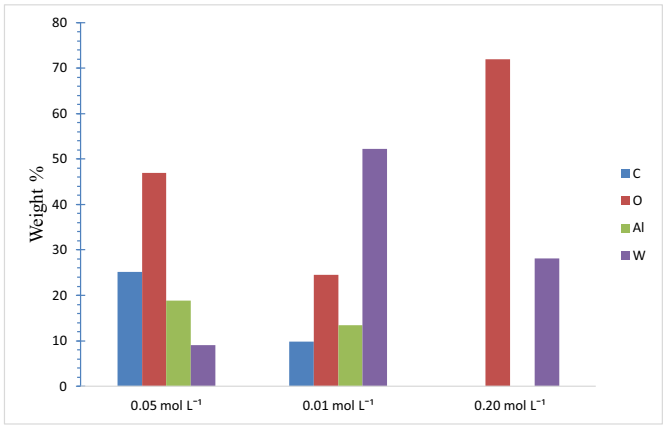

Fig. 3. EDS analysis of Al/WO_3 nanocomposites.

(Fig. 3). Additionally, the particle size of 0.05 mol L^{-1} Al doped was found to be 18.32 nm and as the concentration of the Al dopant increases from 0.1 mol L^{-1} to 0.2 mol L^{-1}, the average particle size reduced from 16.7 nm to 9.4 nm. In the same vein, the HRTEM images in the set of Fig. 2(b), (e) and (h) showed the lattice d spacing as 0.45 nm, 0.41 nm and 0.39 nm, respectively which correspond to (002) crystal planes. The SAED patterns demonstrated the presence of continuous clear ring pattern with little additional spots revealing the polycrystalline structure of the Al doped WO_3 nanoparticles.

3.1.3. XRD analysis of Al doped WO_3 nanoparticles

Fig. 4(b) shows the XRD pattern of WO_3 doped with different concentration of aluminium . The XRD patterns of undoped WO_3 nanoparticles have been previously explained in Fig. 4(b). The XRD pattern of 0.05 mol L^{-1} Al doped WO_3 nanoparticles showed sharp and intense diffraction peaks at angle 2θ value of 24.00°, 28.14°, 42.00°, 50.00° and 58.02° which correspond to the following crystal planes of (020), (200), (202), (100), (110), (210), (300) and (211). These peaks matched with index pattern of monoclinic phase of WO_3 [15.18] with an average crystalline size of 17.3 nm according to Scherer equation. For 0.1 mol L^{-1} Al doped WO_3 nanoparticle, the diffraction peaks were noticed at 2θ value of 23.13°, 24.00°, 24.56°, 28.12°, 14.59°, 28.14° and 28.59°, these peaks correspond to the following crystal planes (020), (200), (100), (110) and (101) and matched with the monoclinic phase of WO_3 [18]. The average particle size was found to be 8.2 nm based on Scherrer equation. The XRD pattern of 0.2 mol L^{-1} Al doped WO_3 nanoparticle revealed the presence of high intense peaks at angle 2θ values of 23.13°, 24.00°, 28.59°, 34.20°, 42.00° and 56.13° which were assigned to the following crystal planes (020), (110), (101), (202). (220). (112) and (300) these peaks matched with the pattern of monoclinic phase of WO_3 whose average crystalline size was 12.02 nm. It can be seen that addition of aluminium did not influence change of WO_3 phase however responsible for the reduction of crystallite size of WO_3.

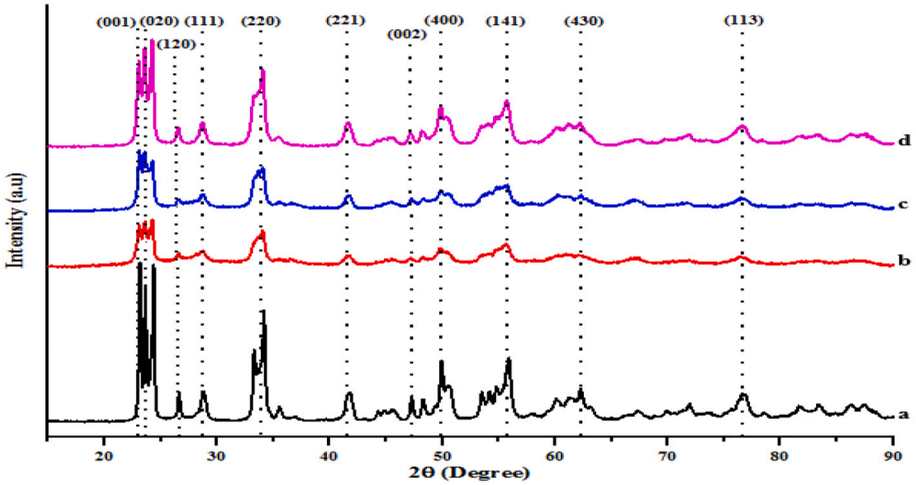

Fig. 4. XRD pattern of WO_3 prepared at different concentrations of aluminium precursor. (a) Undoped WO_3, (b) 0.2 mol L^{-1}, (c) 0.1 mol L^{-1} and (d) 0.05 mol L^{-1}.

3.1.4. HRSEM analysis of B doped WO_3 nanoparticles at different concentration

The HRSEM images of the synthesized Boron doped WO_3 nanoparticles are shown in Fig. 5(a–d).

Fig. 5(a) demonstrates the formation of less agglomerated uniform spherical particles. Unlike Fig. 5(a), it was noticed that when WO_3 nanoparticles was doped with 0.05 mol L^{-1} boron precursor, heterogeneously distributed agglomerated spherical, ring or slate like shape morphology was observed (Fig. 5(b)), Similar trend was observed for 0.1 mol L^{-1} boron doped WO_3 (Fig. 5(c)). The evenly distributed agglomerated slate/ring-like symmetry with small quantity of spherical shapes was observed at higher concentration of 0.2 mol L^{-1} boron precursor; (see Fig. 5(d)). The change of undoped WO_3 from spherical to ring-like morphology due to B addition was based on its small ionic radius (0.23 Å) compared to W and O, which distorted or shrinked the lattice and nanostructure of WO_3 [47]. The average particle size decreases as the concentration of the boron dopant increase due to substitution of W or O atoms with B atoms or probably differences in atomic sizes of the elements. The average crystallite sizes, arranged in ascending order, are 18.7 nm > 13.4 nm > 11.6 nm for 0.05 mol L^{-1}, 0.1 mol L^{-1}, and 0.2 mol L^{-1} B doped WO_3 nanoparticles. Thus, at high concentration of (0.2 mol L^{-1}), more boron penetrated the lattice layer

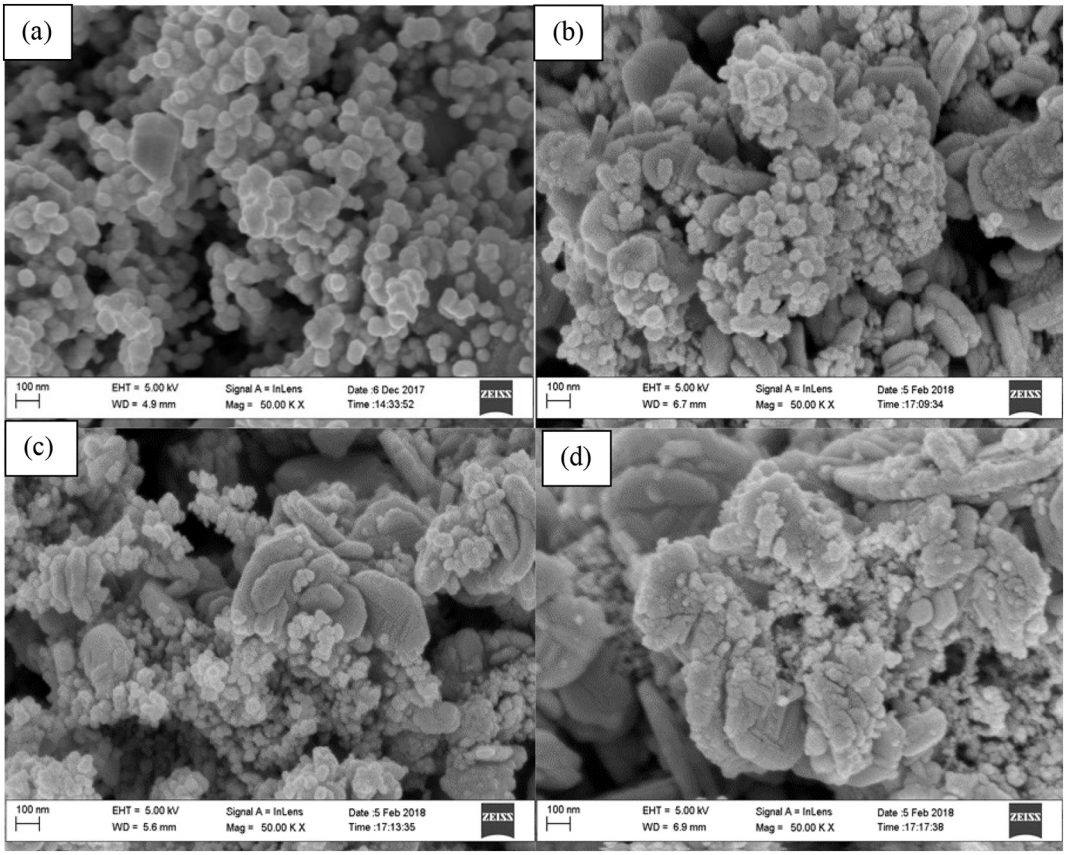

Fig. 5. HRSEM micrograph of undoped and B_2O_3 doped WO_3 nanocomposites (a) undoped WO_3, (b) 0.05 mol L^{-1}, (c) 0.1 mol L^{-1} and (d) 0.2 mol L^{-1} boric acid precursor.

and caused morphological structural changes of WO_3 nanoparticles than when 0.05 mol L^{-1} and 0.1 mol L^{-1} were used.

3.1.5. HRTEM/EDS/SAED analysis of B doped WO_3 nanoparticles

High Resolution Transmission Electron Microscopy (HRTEM) micrographs at high (2 nm) and low (50 nm) magnification and SAED images of the synthesized B-doped WO_3 nanoparticles are shown in Fig. 6.

Fig. 6(a) revealed the presence of evenly distributed agglomerated spherical particles while Fig. 6(d) showed heterogeneous and aggregated spherical and cubic shape. In the case of Fig. 6(g), which is 0.2 mol L^{-1} B doped WO_3 nanoparticles, heterogeneous mixture of spherical and cubic were observed. It can be seen that an increase in the concentration of boron from 0.05 mol L^{-1} to 0.2 mol L^{-1}, was responsible for the morphological transformation from spherical to mixture of spherical and cubic structure. These microstructural changes were ascribed to the diffusion and B substitution of W resulted to distortion and internal stress in the WO_3 host lattice. As the concentration of boron dopant increase to 0.1 mol L^{-1}, the average crystallite size reduced to 8.4 nm and similar trend of size reduction was observed as the concentration increase to 0.2 mol L^{-1} to (average crystallite size 5.6 nm). The reduction of particle size as the concentration of B increases corroborated the findings of [27] and [41]. The HRTEM images in the insets, Fig. 6(b), (e) and (h) show the lattice d-spacing as 0.35, 0.37 and 0.42 nm, respectively which correspond to the (002) interplanar distances and further support planes of monoclinic WO_3. The presence of lattice fringes at high magnification further confirmed that the synthesized materials were highly crystalline, as can be seen in the SAED patterns (Fig. 6(c), 6(f) and 6(i)) which demonstrate the appearance of continuous ring patterns and bright diffraction spots.

Energy dispersive X-ray spectroscopy (EDS) was done to investigate elemental composition of the as-synthesized B doped WO_3 nanoparticles at different concentration of boron and the EDS result is displayed in Fig. 7. The EDS results revealed atomic percentage of tungsten, oxygen, carbon and boron. The level of W reduces as the concentration of the dopant (B) increase while no B was detected. Non-detection of B suggests successful diffusion and penetration of the B onto the inner pores of WO_3 nanoparticles. This is because the ionic radii (0.23 Å) and atomic weight (10.8) of B is smaller than that of W and O. The incorporation of B caused distortion and overlapping of the monoclinic planes of WO_3 and subsequent transformation to ring or plate-like morphology phase, respectively.

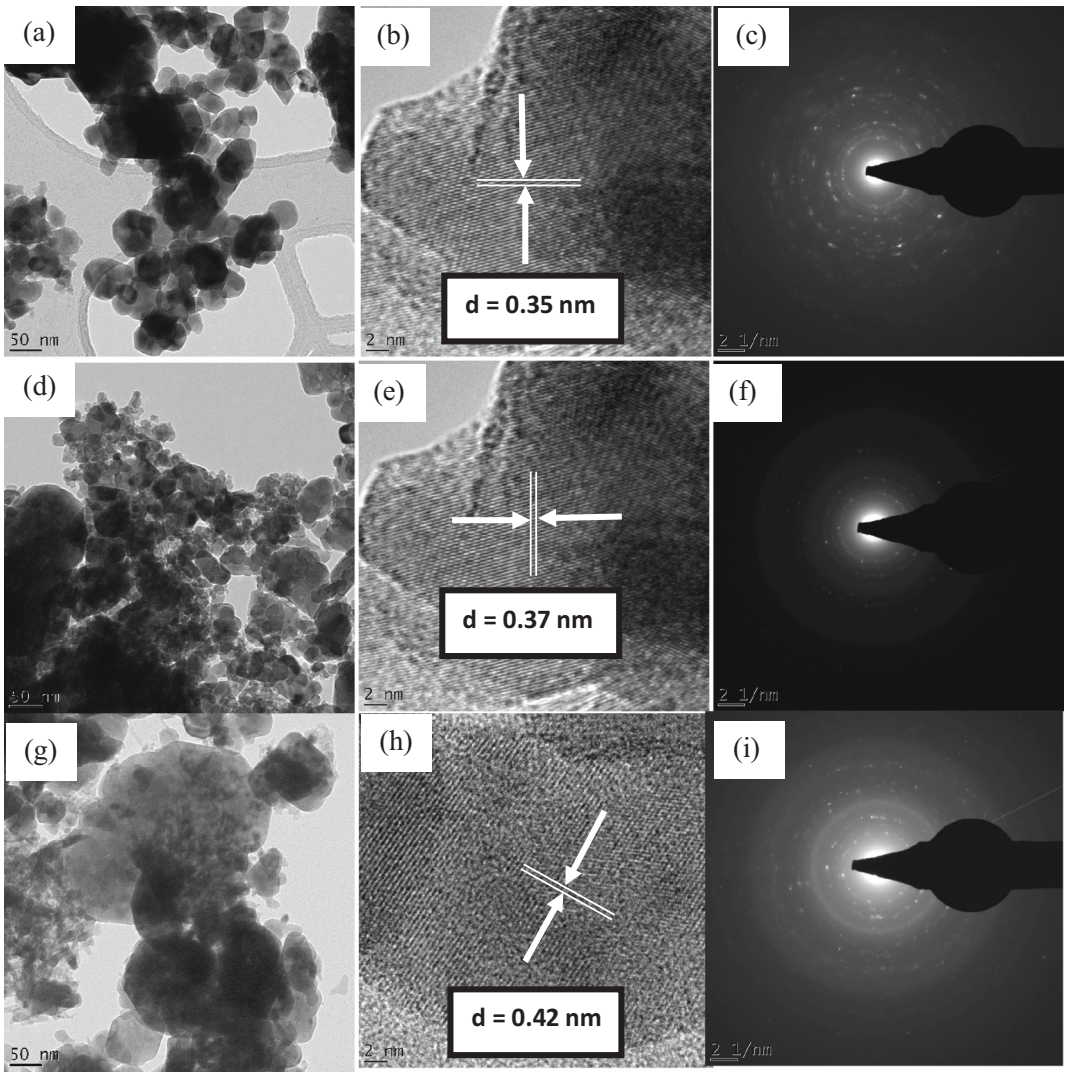

Fig. 6. HRTEM micrograph of WO_3 nanoparticles doped with different concentration of Boron (a) 0.05 mol L^{-1}, (d) 0.1 mol L^{-1} and (g) 0.2 mol L^{-1} at low magnification (50 nm) while (b) 0.05 mol L^{-1}, (e) 0.1 mol L^{-1} and (h) 0.2 mol L^{-1} with different concentration of B with their corresponding SAED images (c), (f) and (i) at high magnification (2 nm).

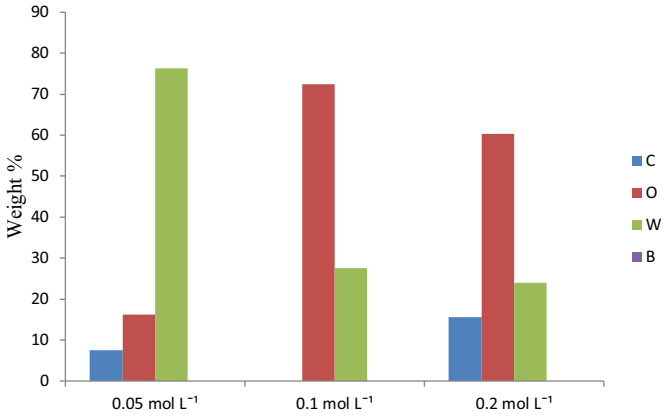

Fig. 7. EDS analysis of B/WO_3 nanocomposites.

3.1.6. *X-ray diffraction analysis of B doped WO_3 nanoparticles*

The XRD patterns of WO_3 nanoparticles doped with different concentrations of boron are shown in Fig. 8(b–d).

The XRD pattern of un-doped WO_3 nanoparticle (a) showed sharp diffraction peaks (001), (020), (200) and (202) crystal plane that correspond to 2θ value of 23.13°, 24.00° and 28.12°, respectively. These diffraction peaks matched with the index pattern of monoclinic phase of WO_3 with the JCPDS card No. 83-0947 and average crystalline size of 17.32 nm [18]. For 0.05 mol L^{-1} B doped WO_3, the diffraction peaks were noticed at 2θ value of 23.13°, 24.00°, 24.56°, 28.12°, 28.14° and 28.59° respectively. These peaks correspond to the following crystal planes (002), (020), (200), (202), (100), (110) and (101) and matched with the monoclinic phase of WO_3 the average particle size was determined to be 14.3 nm. Furthermore, there was no significant difference when 0.1 mol L^{-1} boron precursor was introduced onto the lattice layer of WO_3 nanoparticles, in fact weak diffraction peaks observed at 2θ value of 23.13°, 24.00°, 24.56°, 28.12°, 28.59°, 50.00°, 56.13° and 76.00°. These were ascribed to (002), (020), (200), (202), (110), (101), (221), (311) and (322) crystal planes and depicts the formation of monoclinic phase of WO_3. The average crystallite size was calculated using Scherer equation and found to be 9.2 nm. In the case of 0.2 mol L^{-1} B doped WO_3 nanoparticle, the XRD pattern revealed main characteristics peaks at 2θ value of 14.59°, 23.13°, 24.00°, 28.14°, 28.59°, 28.12°, 42.00°, 56.13° and 76.00° which were assigned to miller indices of (100), (002), (020), (110), (101), (202), (220), (112), (221), (311) and (322). These peaks matched properly with monoclinic WO_3 phase with average crystalline size of 6.4 nm. It can be noticed that slight difference exists in the diffraction pattern of the undoped and B doped WO_3 nanoparticles. Precisely, the peak intensity for monoclinic phase reduced with increasing amount of boron dopant. This clearly support the HRSEM result (Fig. 5(b–d)) as evidence in the morphological transformation from completely spherical shape to ring or plate-like structures. Comparatively, the intensity of the diffraction peaks slightly reduced compared to either by W or O in WO_3 monoclinic because of the smaller ionic radii of B (0.23 Å) than W (2.02 Å) and O (1.207 Å). Although, substitution of W by B is still a subject of further investigation due to the mismatching of oxidation state between B^{3+} and W^{6+} [27]. It is evident that not all the B were involved in doping activities as some formed oxides with its self (B_2O_3) and existed as cluster on the surface of WO_3 nanoparticle (Fig. 5(b–d)). This implies that concentration of boron dopant influenced the morphology and the crystalline sizes of synthesized WO_3, however did not change its phase.

3.1.7. *HRSEM/HRTEM/SAED micrograph of undoped and Al/B doped WO_3 nanoparticles*

The HRSEM/HRTEM/SAED micrograph of the undoped WO_3 and Al/B co-doped WO_3 nanocomposites is shown in Fig. 9. Fig. 9(a) revealed the formation of purely spherical shapes which correspond to monoclinic phase. While in the case of Al/B doped WO_3 nanocomposite partial destruction of the spherical shapes was noticed due to simultaneous diffusion and substitutional mechanism of aluminium and boron resulting to internal structural grain boundaries and stress adjustment of lattice crystal of WO_3 caused by the entity of the two dopants [46,48]. This finding is supported by EDS results of the nanocomposites (Fig. 10). This implies that the changes in shape of WO_3 nanoparticle suggest inner penetration and surface deposition of Al and B based on their equal number of electron. The HRTEM micrographs at high (2 nm) and low (50 nm) magnification and SAED, images are presented in Fig. 9(c–e). The HRTEM image (Fig. 9(c)) demonstrated the presence of dense agglomerated tiny particles due to destruction of spherical morphology observed for undoped WO_3 nanoparticles and may be attributed to the penetration of Al^{3+} and B^{3+} based on their equal number of valence electrons onto the host lattice of WO_3. In addition, the SAED pattern revealed the formation of ring patterns thus suggest that Al/B co-doped WO_3 is of high crystallinity.

3.1.8. *XRD analysis of undoped WO_3 and Al/B doped WO_3 nanocomposites*

Fig. 11 depicts the XRD pattern of undoped WO_3 and Al/B doped WO_3 nanocomposites. The XRD pattern of un-doped WO_3 nanoparticle demonstrated the formation of sharp and intense diffraction peaks at 2θ value of 23.12°, 24.00°, 24.56° and 28.12° which correspond to (002), (020), (200) and (202) crystal plane. These peaks matched well with the monoclinic phase of WO_3 with average crystalline size of 17.32 nm. While the XRD pattern of Al/B doped WO_3 nanocomposites revealed the presence of sharp but weak diffraction peaks at 2θ value of 23.13°, 24.00°, 27.02°, 28.00° 34.02°, 50.00° and 57.00° with the following crystal planes (002), (020), (200), (110), (202), (210), (300) and (221).

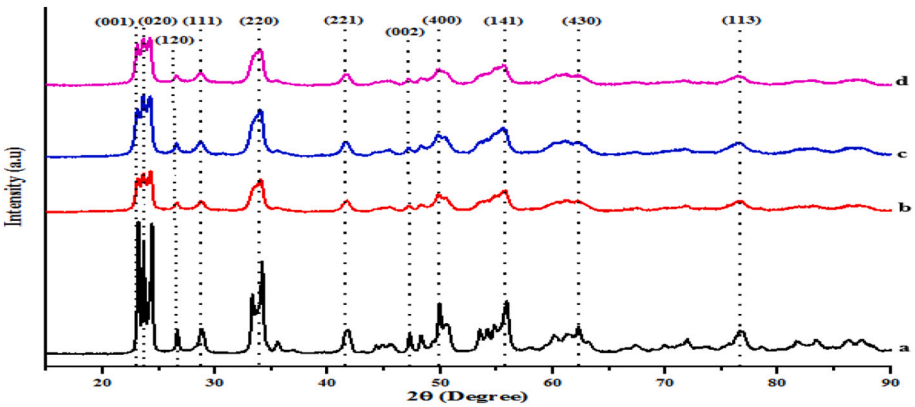

Fig. 8. XRD patterns of the (a) as-synthesized bare WO_3 and (b) 0.05 mol L^{-1}, (c) 0.1 mol L^{-1} and (d) 0.2 mol L^{-1} boric acid precursor doped WO_3.

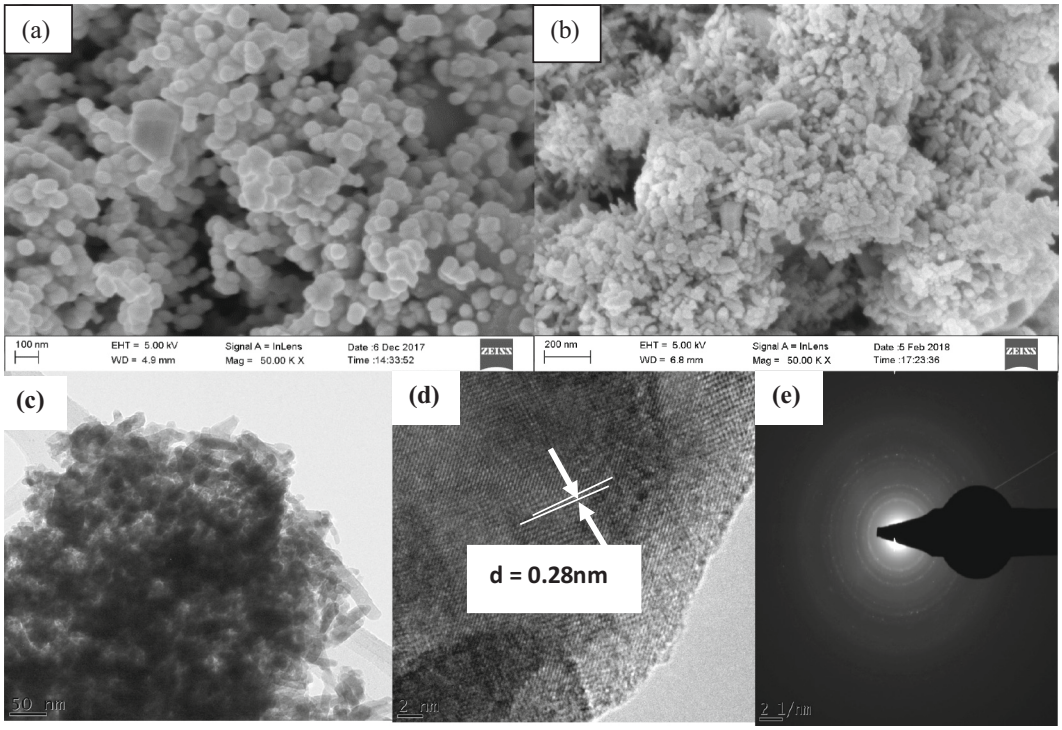

Fig. 9. HRSEM/HRTEM/SAED micrograph of (a) WO_3, (b) aluminium and boron co-doped WO_3 nanocomposite, (c) high magnification, (d) low magnification HRTEM micrograph of Al/B/WO_3 nanocomposites and (e) corresponding SAED images.

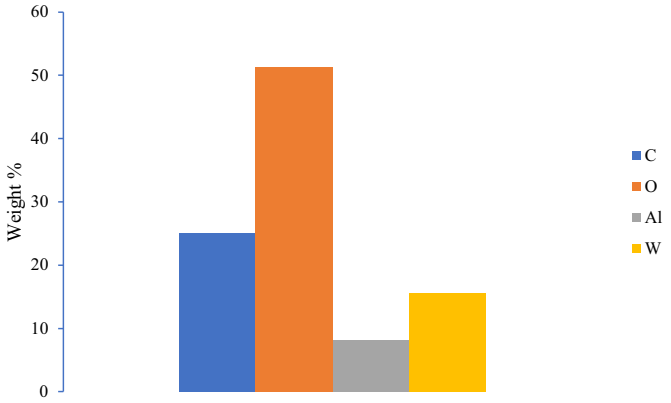

Fig. 10. EDS analysis of Al/B/WO_3 nanocomposites.

These peaks matched properly with monoclinic phase of WO_3 whose average crystalline size was 21.1 nm. The slight increase in particle size may be ascribed to the doping and synergetic effect between the two dopants [18]. None detection of Al or B in the composite material implies that the concentration of the two dopants was low or below the detection limit of the instrument. The addition of the two dopants did not distort the phase of WO_3.

3.1.9. UV–Visible diffuse reflectance analysis and bandgap energy calculation

The UV–Visible diffuse reflectance analysis of WO_3, Al doped WO_3, B doped WO_3 and Al/B doped WO_3 nanocomposites in the wavelength range of 200–800 nm is presented in Fig. 12(a) while Fig. 12(b) depicts the Tauc's plot of the band gap energies of undoped WO_3 and co-doped WO_3 nanocomposites.

As shown in Fig. 12(a), it can be seen that the absorption edge of the UV–visible diffuse reflectance spectra shifted to a higher wavelength (red shift, B/WO_3). The slight red shift observed may be due to the simultaneous doping of Al and B onto the WO_3 nanoparticles. In addition, the red shift may be linked to the charge-transfer transition between the Al and B electrons and the conduction or valence band of WO_3. The electrons transfer occurred between 2p and 5d orbital for B and W; and 3p and 5d orbitals of Al and W respectively. Similar findings were reported by [44] and [45]. The shift from (500–510 nm) to the visible region may be ascribed to the suppression of the rate of recombination of electron/hole pairs in the WO_3 nanoparticles by aluminium and boron. On the contrary, the absorbance edge of the bare WO_3 nanoparticles was approximately at wavelength of 500 nm. While that of the B/WO_3 was less than the ordinary WO_3, which means that for the mono doped material the absorption threshold shifted to a much lower wavelength (<500 nm) due to Burstein-Moss effect and less energetic interaction between electron in 2p orbital of B and electrons in 5d orbital of W [14]. The Al doped WO_3 absorbs at a longer wavelength than WO_3 alone attributable to the doping effect of Al into the interstitial layer of WO_3 based on ionic radius mechanism (Al^{3+} (0.05 nm) and W^{6+} (0.065 nm). The shift to higher wavelength noticed for Al doped WO_3 sample may be linked to strong interaction between energetic 3p electrons in Al and 5d electrons in W. Compared with the undoped WO_3, the absorption bands of Al doped WO_3 and Al/B doped WO_3 nanomaterials were greater than WO_3 alone. This red shifts and enhancement of absorbance of the two materials may be explained based on the basis of simultaneous charge-transition between Al^{3+} and B^{3+} electrons and WO_3 conduction or valence band. The energy band gap (Eg) values were obtained from the absorption coefficient calculated as a function of photon energy (hv). The relationship between the absorption coefficient and photon energy is expressed in Eq. (2).

$$(ahv)^2 = C(hv - Eg) \tag{2}$$

where C is a constant and can be calculated using expression $\alpha = \frac{A}{d}$ where A is the absorbance and d is the thickness of the sample in the UV–Visible cell. The band gap energy of the synthesized nanocomposites was obtained by extrapolating the linear portion of the graph $(\alpha hv)^2$

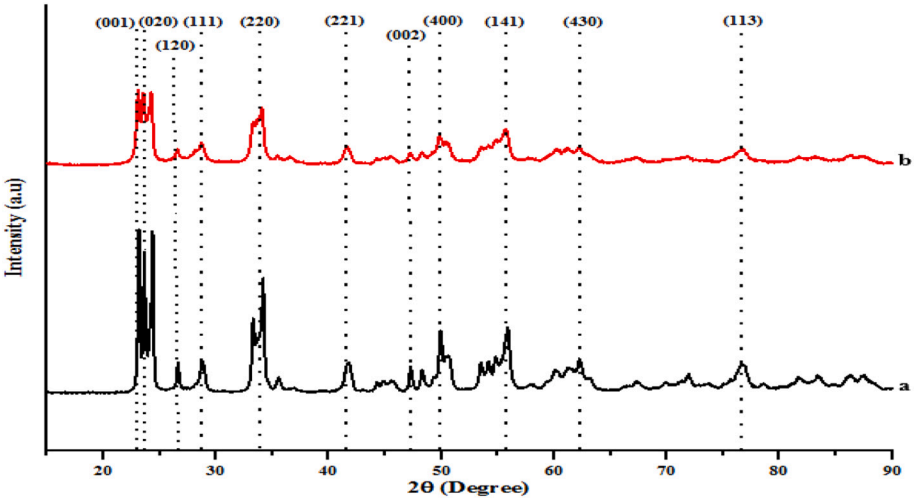

Fig. 11. XRD pattern of (a) undoped WO_3 and (b) Al/B co-doped WO_3 nanocomposites.

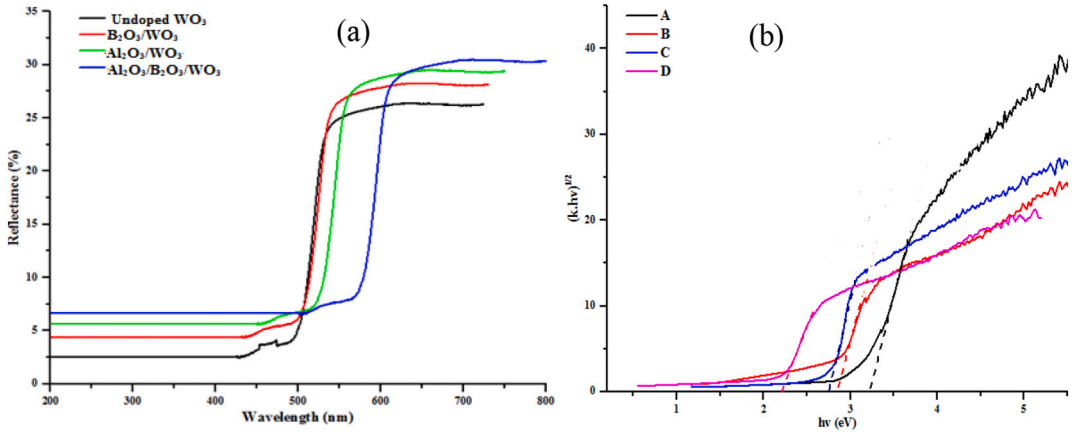

Fig. 12. (a) UV–Visible spectroscopy spectra of WO_3, Al/WO_3, B/WO_3 and Al/B/WO_3 nanocomposites; (b) Tauc's plot of (A) B/WO_3; (B) WO_3; (C) Al/WO_3 and (D) Al/B/WO_3.

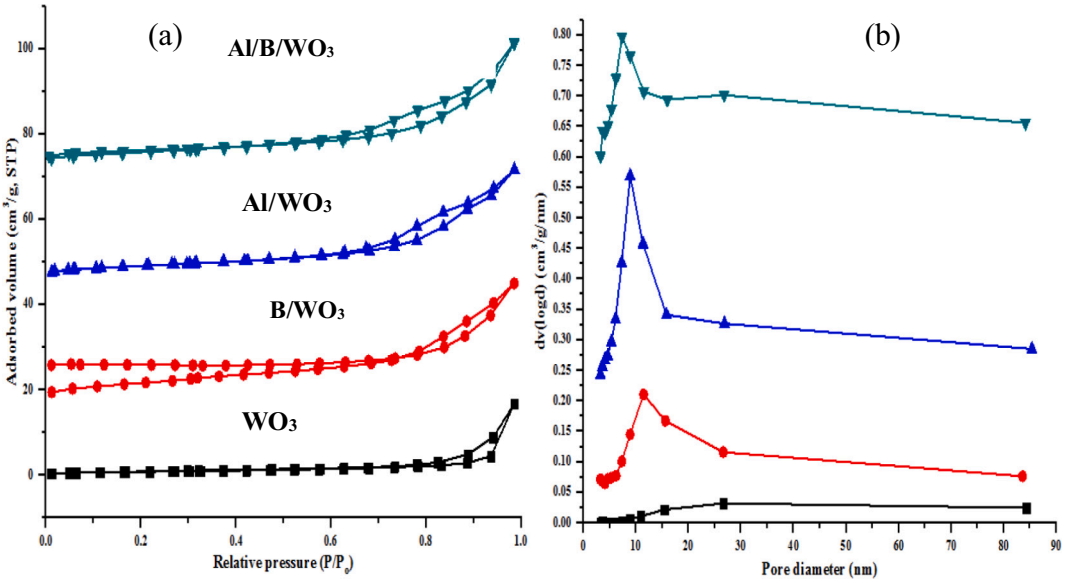

Fig. 13. (a) BET surface area and (b) pore size distribution of WO_3, Al/WO_3, B/WO_3 and Al/B/WO_3 nanocomposites.

versus (hv) as shown in Fig. 12(b). The band gap energy of 2.42 eV for the synthesized WO_3 in this study is lower than 2.61 eV reported by Li et al. [46] who prepared WO_3 via hydrothermal method. WO_3 is an n-type semiconductor with band gap energy in the range of 2.6 eV to 3.2 eV [47]. The differences in the band gap energy may be ascribed to the different method of synthesis and reaction conditions which determined the morphology and the crystalline nature of the material. In addition, doping effect of carbonaceous materials from the plant extract used during the synthesis produced new crystal defects and localized states and as such may be responsible for the lower band gap energy reported in this study. The band gap energy for $B/WO_3 > Al/WO_3 > Al/B/WO_3$ were 2.70 eV > 2.20 eV > 1.7 eV respectively. The reduction in band gap energy of the WO_3 may be due to doping effect of boron and aluminium which increased oxygen vacancies. This suggests that $Al/B/WO_3$ composites with the smallest band gap value may exhibit excellent photocatalytic properties under sunlight than others.

3.1.10. Brunauer Emmett Teller (BET) analysis of the prepared nanomaterials

The specific surface area (m^2/g) and pore size of the synthesized WO_3, Al/WO_3, B/WO_3 and $Al/B/WO_3$ were determined using N_2 adsorption-desorption BET method and corresponding curves is shown in Fig. 13(a) and (b). According to IUPAC, the four samples exhibited a type IV isotherm with an H1-type hysteresis loop linked to open-ended cylindrical pores, an indication of mesoporosity over micro or macroporosity [31]. The pore size distribution of four samples revealed the presence of mesopores with pore diameter in the 3.2–88 nm (see Fig. 13 (b)).

The measured specific surface area and pore size of the prepared nanomaterials is shown in Table 1.

From Table 1, it can be noticed that the surface area of the nanomaterials increased in the order of $Al/B/WO_3 > Al/WO_3 > WO_3$ while an opposite trend was observed for the pore sizes. The BET surface area value of the WO_3 increases slightly when aluminium and boron dopant were mono-doped. However, the introduction of aluminium and boron as co-dopants significantly enhanced the surface area from 22.49 m^2/g to 63.94 m^2/g. The increment in surface area may be due to the intercalation of the $Al^{3+}$and B^{3+} in the lattice structure of the WO_3 [44,47]. Another possible reason may be linked to no change or distortion of the monoclinic phase and the symmetry of the WO_3.

3.1.11. X-ray photoelectron spectroscopy analysis

The elemental composition and the oxidation states of the as-synthesized WO_3, Al/WO_3, B/WO_3 and $Al/B/WO_3$ were determined using XPS and the results are shown in Fig. 14. The following elements: W, Al, O, B and C were obviously present on the surface of the nanomaterial as shown in Fig. 14. A typical high energy resolution spectrum of the W(4f) region is shown in Fig. 15(a).

The 4f energy level splits upon ionization with a spin-orbit splitting ratio for the W $4f_{5/2}$ and W $4f_{7/2}$ levels of 3:4. The fits indicate two doublet peaks. The first set (35.6 and 37.6 eV) corresponds to a W^{6+} stoichiometric WO_3 state and the second (34.2 eV) to W^{4+} while the peak at 36.2 eV is assigned to W^{5+} indicates O-vacancy and/or doped species replacement [17]. The first set of peaks for W at binding energies (35.6 and 37.6 eV) depicts W^{6+}–O bonds in WO_3. The sharp peak at 530.5 eV (Fig. 15(b)) corresponds to the binding energy of O (1s) signify the characteristic peak of lattice oxygen (O^{2-}) in WO_3 [48]. In (Fig. 6b), O 1s peak was located at ~530.5 eV, while in Fig. 15(d), a slight

Table 1
Surface area and pore size of the prepared nanomaterials.

Properties	WO_3	B/WO_3	Al/WO_3	$Al/B/WO_3$
Surface area (m^2/g)	22.49	20.13	32.50	63.94
Pore volume (cm^3/g)	0.104	0.021	0.106	0.157
Pore diameter (nm)	11.42	3.28	16.02	8.85

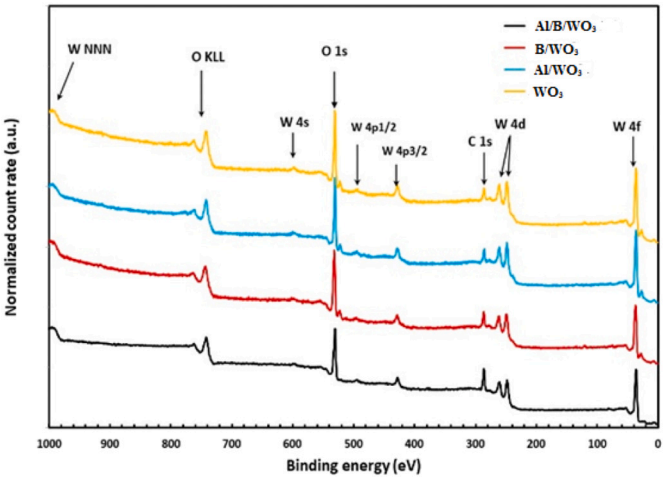

Fig. 14. XPS survey for WO_3, Al/WO_3, B/WO_3 and $Al/B/WO_3$ nanocomposites.

difference in the binding energy in the range of 0.1–0.3 eV, was observed for B/WO_3 and $Al/B/WO_3$ respectively. The shift noticed for O 1(s) in B/WO_3 and $Al/B/WO_3$ is similar to that of W4f peak. The shifting phenomena may be due to relaxation of W atoms due to the removal of an O atom, thereby solidifying the bond of other lattices. The apparent slackening reduced the bond length of W—O including overlapping of other bonds dangling within the framework of W. A shift in binding energies observed in $Al/B/WO_3$ for W 4f and O 1s suggested the existence of strong interaction between W^{6+} and oxygen vacancies. Studies have shown that oxygen removal based on outward motion from the next-nearest-neighbour O in WO_3 often causes compression of bonds by 20 %. Thus, a slight shift noticed for O (1s) and W4f have been ascribed to the presence of oxygen vacancies. Similar phenomenon was observed for (WO_{3-x}) [17]. In the same vein, photoelectron doublet peaks of Al (2s) and Al (2p) were found at the binding energies of 80 eV and 75 eV respectively (Fig. 15(e)) confirmed successful incorporation of Al onto the surface layer of WO_3. This implies that one of the O (1s) has been substituted or replaced by Al. The binding energy peak of B (1s) in the Fig. 15(f) located at 190.5 eV revealed that the boron dopant is in trivalent state (B^{3+}) confirming the successful immobilization of the boron into the lattice structure of the WO_3. In summary, it was observed that the WO_3 sample contain two contributing factors firstly one from W (4f) energy enveloped with a stoichiometric (WO_3) and non-stoichiometric contribution (WO_{3-x}) [31]. The non-stoichiometric (WO_{3-x}) is an indication of O^- vacancies and possible the replacement of the lattice oxygen in WO_3 by the two dopants (Al and B). It is well known, that the presence of C-OH groups on the surface can trap the positive holes and prevent electron-hole recombination, increasing the mobility and lifetime of the photo-generated holes [49]. Closer inspection of the detail XPS-carbon 1 s fits (see Fig. 15(g)–(j)) shows clearly that the $Al/B/WO_3$ specimen has a high C-OH peak (indicated with arrow) compared to the other specimens. This is followed by the Al/WO_3 specimen and the rest has almost no C-OH present. Apart from the surface area and bandgap it looks as if the prevention of electron-hole recombination plays the dominant role in the higher photocatalytic activity of $Al/B/WO_3$.

3.2. Photocatalytic studies

The photocatalytic activity of Al/B doped WO_3 nanoparticles on the degradation of local dyeing wastewater was evaluated under sunlight irradiation. Prior to this, the selected physiochemical parameters of the local dyeing wastewater were determined and the result is shown in Table 2.

Comparing the raw values with the permissible limits set by World

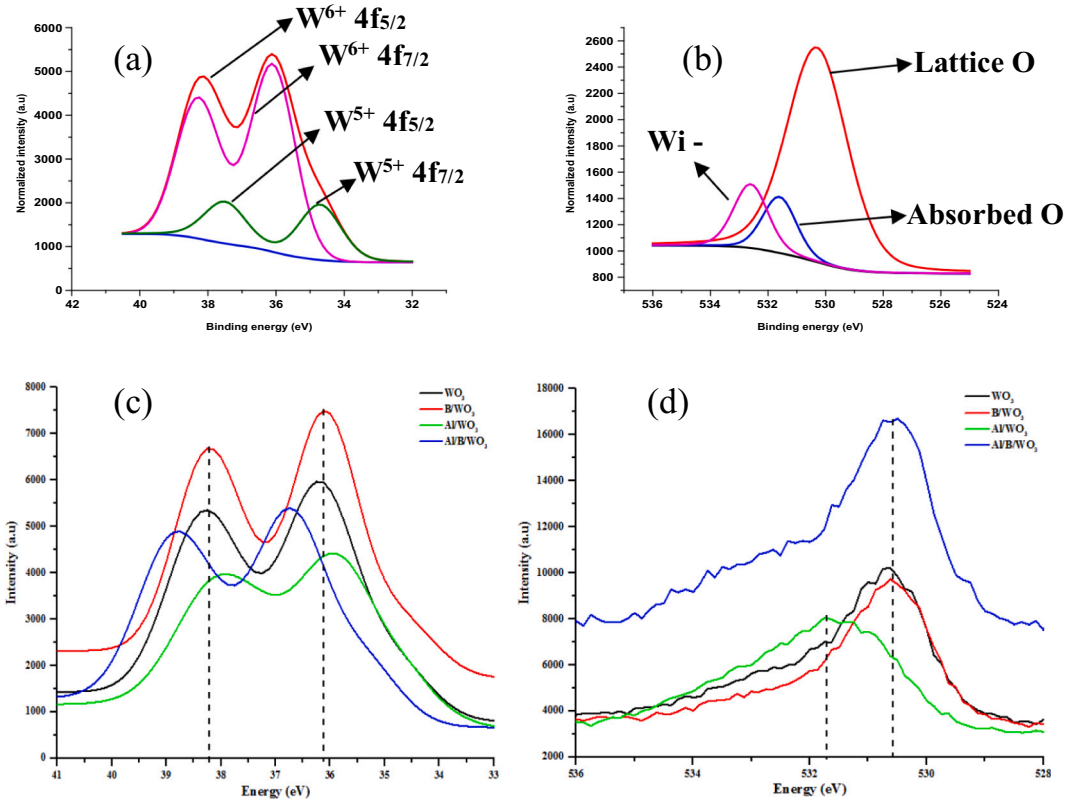

Fig. 15. (a) XPS survey of W ($4f_{7/2}$) and ($4f_{5/2}$) photoelectron peaks; (b) XPS survey of O (1s) region; (c) XPS survey of W in prepared WO_3-x (d) XPS of O in prepared WO_3-x (e) Al (2s) and (2p) region; (f) XPS survey of B (1s) region; (g) XPS survey of C (1s) for WO_3 (h) XPS survey of C (1s) for B/WO_3 (i) XPS survey of C (1s) for Al/WO_3 (j) XPS survey of C (1s) for Al/B/WO_3.

Health Organisation (WHO) [50], it is clear that the collected dyeing wastewater is not safe for both human and aquatic species and therefore must be treated before direct discharge into the environment. The unpleasant odour and colour in the raw dyeing wastewater were ascribed to the presence different organic and inorganic materials such as detergents, fabric whiteners and others used in the dyeing operations. The pH value of the raw wastewater was 9.5, which mean the wastewater is alkaline and slightly higher than the recommended value by WHO [50], and higher value of pH may be linked to excessive use of carbonates, bicarbonates, sodium hydroxide and bleaching compounds during bleaching process which increase the toxicity. Not only that, the TDS value is also high above the permissible limit which suggests high amount of suspended solids in the water used during the dyeing operation [51–52]. High amount of suspended solids is problematic for treatment and thus the collected wastewater was subjected to filtration before photocatalytic process. According to Reddy and Osborne [53], electrical conductivity (EC) is the potential of chemical substances to possess electrons and this depends on amount of ionic salts and dissolved solids. In this case, it was found that the EC of untreated and treated wastewater selected was less than the permissible limits (1000–2000 $\mu m^2/cm$). High amount of EC in water did not support the survival of aquatic species. Based on the initial BOD, TOC and COD value, it can be inferred that the wastewater contains several toxic organic and inorganic compounds, which must be decomposed into CO_2 and H_2O. Table 2 also shows that the dyeing wastewater contain several anions and cations, with sulphate as the predominant. These anions and cations are classified as radical scavengers, which compete with hydroxyl radicals during photocatalytic oxidation of dyeing wastewater.

Table 2 also reveals the presence of five toxic heavy metals and the order of occurrence of the metals were Zn > Cr > Fe > Ni > Pb. This means zinc was the most abundant metal and may be ascribed to high mineral content in water used during dyeing operation. Similar observation was reported by [50–52]. Exposure to each of the metals has been linked to different health challenges. For instance, chromium toxicity can cause liver and kidney disorders while cumulative effect of Pb in the body can result to hypertension, neurological disorders amongst others.

Table 2 shows significant reduction of the indicator parameters in the presence of WO_3, mono-doped WO_3 and co-doped WO_3 under sunlight irradiation. The co-doped WO_3 behaved better than undoped WO_3 and mono-doped WO_3 in removal of indicator parameters in dyeing wastewater and the obtained results were lower than the permissible limit of WHO standard [50] (see Table 2). It was noticed that the level of conductivity of the treated water is significantly higher than untreated wastewater, which suggest the presence of anions and cations in the former than the latter. This is an evidence of partial degradation of the organic compounds in the wastewater into harmless species due to their competition with free reactive species for the binding sites during catalytic reaction under sunlight. It was generally observed that the concentrations of heavy metals reduced significantly after the photocatalytic treatment of local dyeing wastewater with the prepared nanomaterials. The decrease in the amount of heavy metals in the treated water suggests that, the prepared nanomaterials also performed as nanoadsorbent. It was also noticed that the decrease in the indicator parameters was nanocatalysts dependent. The biodegradability of effluent in terms of BOD/COD is greater than 0.6, when compared to BOD/COD of less than 0.4 reported by Ramos et al. [54]. This suggests that the treatment of the dyeing wastewater can be conveniently done using promising physicochemical method such as photocatalysis for the removal of COD and TOC [54]. The reductions of the indicator parameters especially COD and TOC in the local dyeing wastewater under the influence of the nanocatalysts as a function of irradiation time under natural sunlight using Eq. (3) is shown in Fig. 16(b) and (c), respectively.

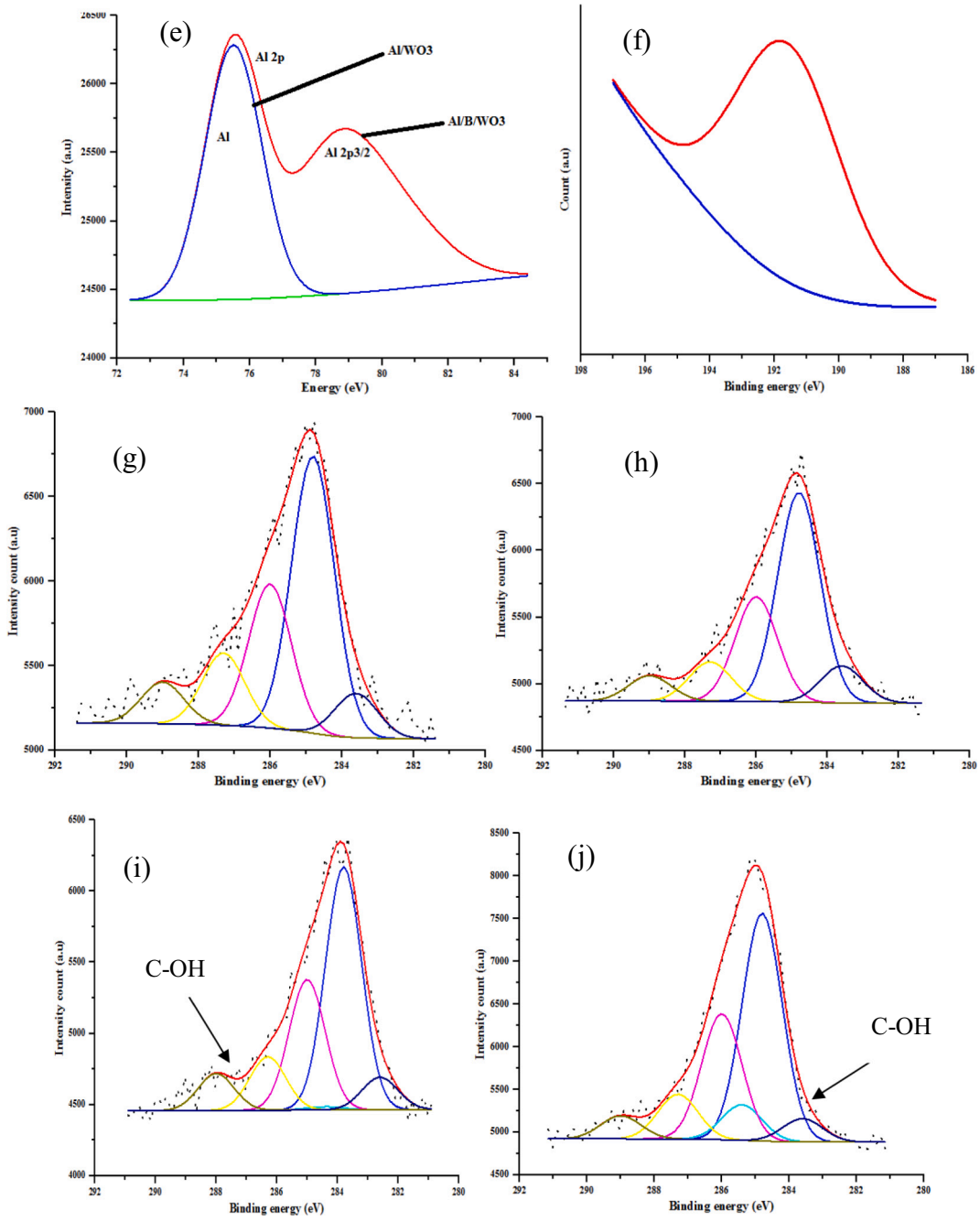

Fig. 15. (*continued*).

$$\text{Percentage removal}\ (\%) = \frac{C_o - C_t}{C_o} \times 100 \quad (3)$$

where C_o and C_t are initial and residual concentrations of COD and TOC at different intervals of irradiation, respectively.

The raw indigenous textile wastewater collected from different pits at the sampling site at different dilution ratios (1%, 5%, 10%, 50% and 70%) were subjected to UV–Visible spectroscopic analysis (Fig. 16(a)). The UV–Visible spectra of a dark and light blue colouration revealed appearance of broad peak of maximum absorbance in the range of 619–640 nm. This suggests that the dyes used by the locals belong to 7-aryl-substituted rhodamines groups [53]. No noticeable peak was observed for 1%, 5% and 10% dye solution due to the dilution effect.

It was noticed from Fig. 16(b) and (c) that the concentration of these indicator parameters (COD and TOC) did not change significantly either under natural sunlight irradiation or in the presence of catalyst alone which mean that the degradation of these dye molecules did not follow photolysis and adsorption pathways. It can be noticed from the two Figs. that the degradation efficiency of the organic compounds based on the indicator parameters increases with increasing irradiation time. This implies that there is an existence of a direct linear relationship between the nanocatalysts and irradiation time. For instance, the reduction of COD value of the dye molecules at 240 min was in the order B/WO_3 (78.9%) < WO_3 (85.0%) < Al/WO_3 (89.4%) < $Al/B/WO_3$ (94.0%). Under the same applied conditions, the TOC reduction level occurred as follows: 68.9% < 73.4% < 80.9% < 90.0% for the following photocatalysts B/WO_3 < WO_3 < Al/WO_3 < $Al/B/WO_3$. It is obvious that the degradation rate of $Al/B/WO_3$ for both parameters was faster than other catalysts under the same applied conditions. The differences in the photocatalytic behavior of the synthesized materials can be explained in

Table 2
Physiochemical parameters and acute toxicity units of raw and treated local dyeing wastewater.

Parameters	Raw values	Treated with B/WO_3	Treated with undoped WO_3	Treated with Al/WO_3	Treated with Al/B/WO_3	Standard WHO, [50]
Colour	Dark-blue	Light blue	Slightly colourless	Slightly colourless	Completely colourless	Colourless
Odour	Offensive	Slightly offensive	Not offensive	Not offensive	No odour	Odourless
Temperature (°C)	32.03 ± 0.45	31.08 ± 0.02	30.21 ± 1.13	32.11 ± 1.18	35.54 ± 0.08	–
pH	9.50 ± 0.11	7.00 ± 1.02	6.80 ± 1.10	6.50 ± 1.57	7.10 ± 1.42	6.0–9.0
TDS (mg/L)	873.01 ± 3.02	735.14 ± 3.78	678.76 ± 4.37	620.21 ± 3.36	430.02 ± 3.78	500
Electrical Conductivity μm^2/cm	633.83 ± 1.62	804.05 ± 2.67	863.20 ± 1.80	814.32 ± 2.11	719.31 ± 1.95	1000–2000
COD (mg/L)	378.00 ± 1.35	57.01 ± 1.78	26.22 ± 1.53	21.19 ± 1.93	10.00 ± 1.76	30
BOD (mg/L)	228.30 ± 2.09	48.19 ± 2.68	22.45 ± 2.13	15.56 ± 3.28	8.84 ± 2.22	<50
Turbidity (NTU)	72.12 ± 3.04	57.32 ± 4.00	14.70 ± 3.96	10.81 ± 3.95	3.22 ± 0.15	5
TOC (mg/L)	623.22 ± 1.22	104.15 ± 1.72	92.40 ± 1.53	56.30 ± 1.67	21.24 ± 1.71	<75
SO_4^{2-} (mg/L)	302.34 ± 1.11	133.24 ± 1.08	102.56 ± 1.54	99.09 ± 1.20	57.89 ± 1.11	800
NO_3^- (mg/L)	238 ± 0.78	198.19 ± 0.66	100.24 ± 0.56	56.48 ± 1.18	15.78 ± 0.56	20
Cl^- (mg/L)	156 ± 1.67	101.45 ± 1.89	86.17 ± 1.60	42.44 ± 1.45	18.67 ± 0.99	600
PO_4^{3-} (mg/L)	24.14 ± 1.35	17.23 ± 1.30	11.57 ± 2.32	8.03 ± 1.11	2.29 ± 1.01	10
Zn^{2+} (mg/L)	1.22 ± 0.55	0.98 ± 0.40	0.60 ± 0.28	0.42 ± 0.10	0.15 ± 0.33	3
Fe^{2+} (mg/L)	1.04 ± 0.04	0.78 ± 0.08	0.66 ± 0.05	0.25 ± 0.01	0.1 ± 0.03	0.3
Cr^{6+} (mg/L)	1.16 ± 0.12	1.11 ± 0.16	0.98 ± 0.02	0.08 ± 0/02	<0.02	0.1
Ni^{2+} (mg/L)	1.00 ± 0.05	0.62 ± 0.02	0.13 ± 0.01	0.04 ± 0.01	<0.001	0.02
Pb^{2+} (mg/L)	0.81 ± 0.02	0.33 ± 0.08	0.10 ± 0.01	0.03 ± 0.01	<0.001	0.01
Toxic unit (TU)	5.40 ± 0.99	1.10 ± 0.08	0.80 ± 0.06	0.38 ± 0.04	0.22 ± 0.01	
Toxicity class	Class III (acute toxicity)					

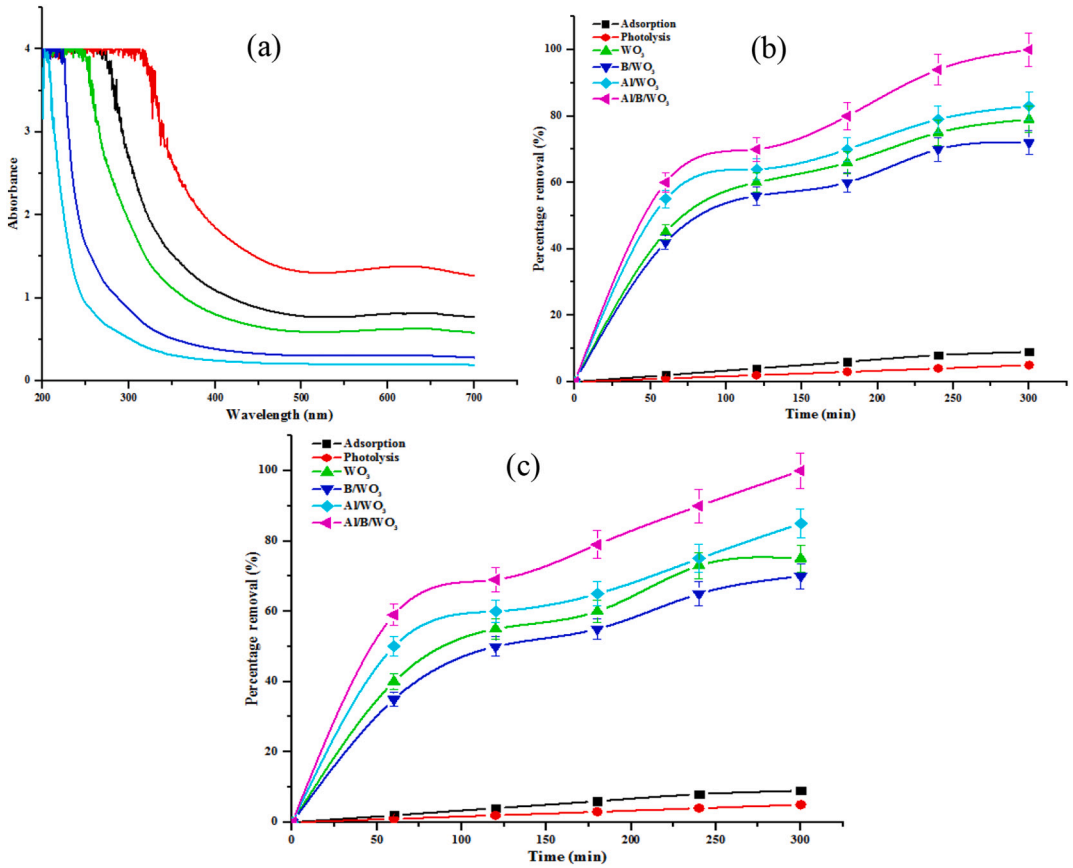

Fig. 16. (a) UV–Visible spectra of 1%, 5%, 10%, 50% and 70% raw local dyeing wastewater, (b) COD reduction from local dyeing wastewater using WO_3, B/WO_3, Al/WO_3, Al/B doped WO_3 nanoparticles, (c) TOC from local dyeing wastewater using WO_3, B/WO_3, Al/WO_3, Al/B doped WO_3 nanoparticles (experimental conditions; catalyst dosage 0.05 g, vol of wastewater 100 mL).

terms of suppression of the electron-hole recombination rate of WO_3 by the two dopants [9]. The higher photocatalytic activity of the Al/B/WO_3 nanocomposites with respect to the mono doped and undoped WO_3 can also be interpreted in terms of the two added dopants having different energy levels for their corresponding conduction and valence band [15–16]. This resulted to the higher interfacial charge transfer efficiency from the dopants to the semiconductor metal oxide, leading to faster electron-hole separation and higher photocatalytic activity. The

differences in the overall activity of the nanocatalysts can also be attributed to the loose structural morphology, a high surface area (evidence of more active and binding sites), moderate band gap energy and surface hydroxyl groups. For instance, Al/B/WO_3 with the smallest band gap energy (1.7 eV) and higher surface area (533.94 m^2/g) exhibited better photocatalytic performance than other catalysts due to the existence of synergetic effect between the two dopants in the composite [17–18]. In the same vein, our results also indicate that Al/WO_3 performed better than B/WO_3 and undoped WO_3 under the same conditions. The observed trend can be linked to smaller band gap energy of 2.20 eV (Al/WO_3) than 2.42 eV (WO_3) and 2.70 eV (B/WO_3) [14]. This implies that nanocatalyst with the lowest band gap prevented the electron-hole recombination rate than other and hence responsible for the observed higher photocatalytic activity. A close observation of the degradation performance showed higher activity for undoped WO_3 than B/WO_3. This suggests that the content of boron may be responsible for the observed decreased surface area and the photoactivity. Whereas, the doping effect of carbonaceous material from the plant extract onto the frame structure of WO_3 enhanced its high oxidation potential under natural sunlight than B/WO_3 material [14]. Additionally, carbon is neither strong electronegative nor electropositive and thus suppress and retard the promoted and transferred electrons from the valence band to conduction bands of WO_3 surface based on lower Fermi Level mechanism [14]. This phenomenon usually created a Schottky barrier at the interface between WO_3 and carbon, which enable free movement of the photo-generated electrons from WO_3 surface towards the carbon surface. Not only that, the recombination rate of photo-generated electrons and holes may be prevented by carbon and as a result favoured enhancement of photocatalytic activity. This finding agreed with the previous studies reported by Hang et al. [45] where 5% Fe-WO_3 exhibited greater photocatalytic efficiency of 93% at an irradiation time of 300 min under visible light irradiation than the undoped alone. The performance of the nanocatalysts prepared previously was compared with this present study in Table 3.

According to Table 3, it can be noticed that the photocatalytic behavior of the nanocatalyst depend on the nature of the pollutants, surface area and the band gap energy. It was found that the catalyst prepared in this study performed better than other catalysts except WO_3 reported by Wang et al. [26]. The differences could be ascribed to the nature of the pollutants while this study used real environmental sample containing several organic compounds, Wang et al. [26] used simulated solution which did not contain any radical scavengers or suspended solids. Again, competition for active sites by the organic compounds is limited in the simulated solution compared to real environmental sample used. Generally, it was found that the physicochemical parameters of the raw wastewater reduced considerably after treatment with the various synthesized nanocatalyst. The behavior of the nanocatalysts may be linked to the surface area and surface adsorbed functional groups.

3.2.1. *Kinetics studies of the photodegradation of local dyeing wastewater by WO_3 photocatalysts*

The experimental data obtained from the photodegradation of organic compounds in the local dyeing wastewater was fitted into three different kinetic models namely: Pseudo-first order, Pseudo-second order and Modified Freundlich as presented Eqs. (4) to (6). The results expressed in terms of correlation coefficient (R^2), rate constant (k), error functions (SSE and X^2) are shown in Tables 4 and 5 respectively.

$$ln\left(\frac{C_o}{C_t}\right) = -kt \tag{4}$$

$$\frac{1}{C_t} = kt + \frac{1}{C_o} \tag{5}$$

$$C_t = kC_o t^{1/m} \tag{6}$$

where C_o and C_t are initial and final concentration of the organic compounds in dyeing wastewater, t is the reaction time (min), k is the rate constant and m is a constant.

According to Tables 4 and 5, it is evident that the experimental data best fitted to pseudo-first order compared to other models based on the value of correlation coefficient (R^2) and rate constant (k) for all the

Table 3
Comparison of the photocatalytic performance of the previous and present study.

Nanocatalyst	Applied reaction conditions for photodegradation of organic pollutants	Photocatalytic properties (band gap, surface area)	Degradation efficiency (%) in term of TOC/COD	References
Dy-doped tungsten trioxide (WO_3) nanopowders	Model pollutant (Rhodamine blue (RB)), concentration and volume of RB solution (CO = 1.0 × 10–5 mol L^{-1}, 30 ml), Ultraviolet source was a 250 WHg lamp, pH of RB solutions (5.8), catalysts dosage (40 mg), reaction time (180 min)	Bare monoclinic phase WO_3 (10.3 m^2/g), 0.05 mol L^{-1} Dy/WO_3 (10.0 m^2/g), 0.25 M Dy/WO_3 (10.5 m^2/g)	WO_3 (66.3%), 0.25 M Dy doped WO_3 nanoparticles (91.2%)	[58]
WO_3 nanoparticles	Model pollutant (Methylene blue (MB)), concentration and volume of MB solution (co = 10 mg L^{-1}, 100 ml), ultraviolet source was a 125 W lamp, pH of MB solution (6.8), catalysts dosage (50 mg), reaction time (60 min)	Mixed phase of monoclinic and orthorhombic WO_3. The surface area and bandgap energy were not calculated	WO_3 (100%) within 60 min	[26]
Ag/WO_3 nanocomposites	Model pollutant (Methylene blue (MB)), concentration of aqueous MB (10 mg L^{-1}), volume of MB solution (200 mL), 150 W high pressure mercury lamp, reaction time (120 min), natural pH of MB solution, catalysts dosage (2 g L^{-1})	Pure monoclinic phase WO_3 (3.00 eV), 3% Ag.WO_3 (2.94 eV), 10% Ag/WO_3 (2.85 eV)	71, 75, and 85% for undoped WO_3 3% and 10% Ag doped WO_3 nanoparticles	[20]
Nb/WO_3 nanomaterials	Model pollutant (Methylene blue (MB)), concentration of aqueous MB (10 mg L^{-1}), volume of MB solution (100 mL), 300 W high-pressure mercury lamp, reaction time (150 min), natural pH of MB solution, catalysts dosage (50 mg)	Pure monoclinic phase WO_3 (2.83 eV, 19.42 cm^3/g), 0.03 M Nb/WO_3 (2.62 eV, 112.71 cm^3/g)	55% for undoped WO_3, 85% for NB/WO_3	[47]
Pt doped WO_3 nanoparticles	Model pollutant (Ethylene), concentration of Ethylene (50 ppm), volume of Ethylene solution (100 mL), 300 W high-pressure mercury lamp, reaction time (60 min), catalysts dosage (66 mg)	Mixture of monoclinic, hexagonal and orthorhombic WO_3 phase (2.75 eV, 8.3 m^2/g), Pt/WO_3 (2.68 eV, 44.4 m^2/g)	Undoped WO_3 (10%), Pt doped WO_3 (28%)	[35]
WO_3 nanoparticles	Model pollutant (Methylene blue (MB)), concentration of MB (20 mg L^{-1}), volume of MB solution (100 mL), Heraeus TQ 150 Hg lamp, reaction time (8 h), catalysts dosage (2 g L^{-1}), varied pH (5, 7, 9, 12)	Monoclinic phase of WO_3 (2.78 eV, 12.1 m^2/g), commercial monoclinic phase of WO_3 (2.76 eV, 11.1 m^2/g)	Commercial WO_3 (32%), synthesized WO_3 (60%)	[59]
WO_3	Local dyeing wastewater (mixtures of organic compounds), concentration of TOC, COD (378 mg L^{-1}, 623.2 mg L^{-1}), volume of wastewater (100 mL), natural sunlight, reaction time (6 h), catalysts dosage (1 g), natural pH (7.2)	Monoclinic WO_3 (2.42 eV, 352.49 m^2/g)	WO_3 (73.4%, 85%)	This study
B/WO_3		Monoclinic WO_3 (2.70 eV, 334.76 m^2/g)	68.9%, 78.9%	This study
Al/WO_3		Monoclinic WO_3 (2.20 eV, 392.50 m^2/g)	80.9%, 89.4%	This study
Al/B/WO_3		Monoclinic WO_3 (1.7 eV, 533.94 m^2/g)	90%, 94%	This study

Table 4
Pseudo first-order, pseudo second-order and modified Freundlich kinetic models for photocatalytic degradation of local dyeing wastewater (TOC as indicator parameter) by WO_3, Al/WO_3, B/WO_3 and Al/B/WO_3 nanocomposites.

Nanoparticles	Parameters	Kinetic models		
		Pseudo first order	Pseudo second order	Modified Freundlich
WO_3	k (min^{-1})	0.106	0.084	0.081
	R^2	0.934	0.912	0.921
	SSE	0.534	2.036	1.593
	X^2	1.201	1.845	1.305
Al/WO_3	k (min^{-1})	0.117	0.100	0.090
	R^2	0.965	0.924	0.913
	SSE	0.355	1.438	1.964
	X^2	1.183	1.216	1.583
B/WO_3	k (min^{-1})	0.100	0.067	0.072
	R^2	0.869	0.830	0.854
	SSE	0.720	1.541	1.220
	X^2	1.252	1.455	1.302
Al/B/WO_3	k (min^{-1})	0.196	0.112	0.095
	R^2	0.998	0.944	0.980
	SSE	0.140	1.319	1.051
	X^2	1.006	1.287	1.113

Table 5
Pseudo first-order, pseudo second-order and modified Freundlich kinetic models for photocatalytic degradation of local dyeing wastewater (COD as indicator parameter) by WO_3, Al/WO_3, B/WO_3 and Al/B/WO_3 nanocomposites.

Nanoparticles	Parameters	Kinetic models		
		Pseudo first order	Pseudo second order	Modified Freundlich
WO_3	k (min^{-1})	0.125	0.107	0.091
	R^2	0.911	0.905	0.921
	SSE	0.038	0.056	1.650
	X^2	1.377	2.390	1.896
Al/WO_3	k (min^{-1})	0.187	0.114	0.118
	R^2	0.998	0.914	0.913
	SSE	0.027	0.051	2.005
	X^2	0.912	1.110	1.206
B/WO_3	k (min^{-1})	0.117	0.102	0.088
	R^2	0.090	0.910	0.918
	SSE	0.086	0.054	2.270
	X^2	1.518	1.993	1.325
Al/B/WO_3	k (min^{-1})	0.202	0.119	0.122
	R^2	0.938	0.944	0.937
	SSE	0.020	0.030	2.530
	X^2	0.782	0.221	0.464

synthesized materials. Besides correlation coefficient (R^2), error functions such as SSE and X^2 were also used to adjudge the best fitted model to kinetic data, and values closer to zero depicts a significant agreement between the experimental and theoretical values. The fitness followed the order of Al/B/WO_3 > Al/WO_3 > WO_3 > B/WO_3 for both TOC and COD in the local dyeing wastewater. Again, the performance of the nanocatalysts may be due to the high surface area and the low band gap of Al/B doped WO_3 than other catalysts. This suggests that the decomposition process of the organic compounds in the local dyeing wastewater by the synthesized photocatalyst is monolayer in nature and depends only on one factor. The reduction of TOC or COD in the local dyeing wastewater depends only on the concentration of the organic compounds. Additionally, the degradation mechanism of the organic compounds is adsorption-desorption controlled. Not only that, the photocatalytic mineralization of the dye molecules occurred mostly on the surface of WO_3 nanoparticles. The differences in the rate constant may be linked to the nature of catalyst, method of preparation of the catalyst, surface area and band gap energy.

3.3. Mechanism of Al/B doped WO_3 photocatalysts

The improved catalytic efficiency of Al/B/WO_3 for the degradation of local dyeing wastewater has been linked to the production of the four reactive species: namely O_2^- (superoxy anion), $^{\bullet}OH$ (hydroxyl radical), e−, and h^+ [14,38]. During the photocatalytic reactions, the organic compounds in the wastewater were adsorbed on the surface of Al/B/WO_3 followed by excitation of the dye molecules. The electron in the valence band moved to the conduction band of pure WO_3 thus creating an electronic vacancy or hole in the valence band. In case of Al doped WO_3, the W^{6+} lattice position was replaced by Al^{3+} ions and then lowered the conduction band of WO_3. On the contrary, addition of B increased the band gap energy of WO_3 due to Burstein-Moss effect (see Fig. 17) [14]. The roles played by the dopants on the enhancement of TOC and COD reduction differ and are explained as follows: Al^{3+} in the composite promoted charge carrier separation efficiency causing migration of Al^{3+} to the catalyst surface for O_2 photoadsorption. Boron also accelerated the activity of WO_3 under natural sunlight through formation of some favorable local structures and surface-active sites during photocatalytic reactions. Under the influence of natural sunlight irradiation, photogenerated electrons from Al reach WO_3 via B or from B to WO_3 via Al. The photogenerated electrons in Al/B oxidizes very rapidly to form superoxy anion (O_2^{*-}) radicals; whereas the holes react with water molecules to produce hydroxyl (OH*) radicals [55]. $^{\bullet}OH$ is primarily generated via oxidative paths, after which, due to its strong oxidizing ability. These two radicals react with the dye molecules and eventually produced some intermediates, CO_2 and H_2O. The bandgap energy of pure WO_3 was lowered by the addition of Al^{3+} and B^{3+} onto the lattice layer of W (see Fig. 17). The two dopants capture electrons during photocatalytic process and as a result, recombination of electron–hole pair was suppressed and hence enhanced the photocatalytic activity for Al/B doped WO_3. Moreover, the smaller bandgap energy due to Al/B dopant can play another role in enhancing the visible light photocatalytic activity of WO_3 catalyst. The proposed reaction mechanisms for the degradation of organic compounds by Al/B doped WO_3 under natural sunlight irradiation are presented in Fig. 17 and Eqs. (7) to (17).

$$Al - B - WO_3 + hv \rightarrow eCB^- + hVB^+ \quad (7)$$

$$H_2O \rightarrow OH^- + H^+ \quad (8)$$

$$hVB^+ + H_2O \rightarrow OH^{\circ} + H^+ \quad (9)$$

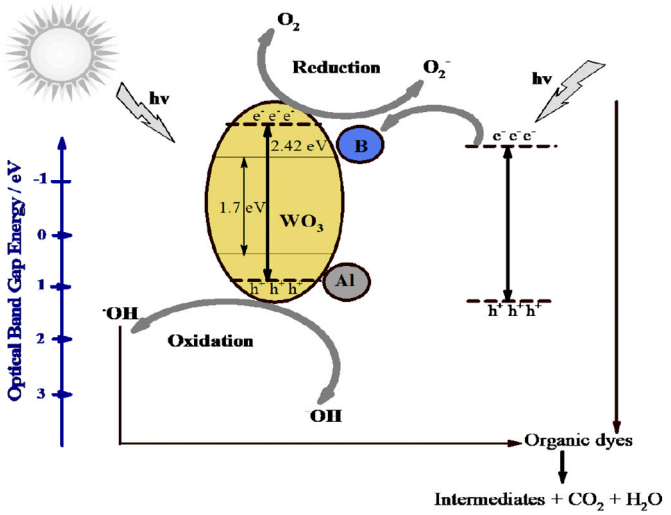

Fig. 17. Proposed mechanism of degradation of local dyeing wastewater by ternary Al/B/WO_3 nanocomposites.

$$hVB^{+} + OH^{-} \rightarrow OH^{\circ} \quad (10)$$

$$eCB^{-} + O_2 \rightarrow O_2{}^{*-} \quad (11)$$

$$O_2{}^{*-} + 2H^{+} + eCB^{-} \rightarrow H_2O_2 \quad (12)$$

$$O_2{}^{*-} + H^{+} \rightarrow HO_2{}^{*-} \quad (13)$$

$$HO_2{}^{*-} + HO_2{}^{*-} \rightarrow H_2O_2 + \frac{1}{2}O_2 \quad (14)$$

$$H_2O_2 + H^{+} + eCB^{-} \rightarrow OH^{\circ} + H_2O \quad (15)$$

$$OH^{\circ} + \text{organic dyes} \rightarrow \text{intermediates} + H_2O + CO_2 \quad (16)$$

$$O_2^{\cdot -} + \text{organic dyes} \rightarrow \text{intermediates} + H_2O + CO_2 \quad (17)$$

3.4. Toxicity test of local dyeing wastewater to Daphnia magna

Table 2 shows that acute toxicity conducted on untreated local dyeing wastewater using *D. magna* indicator was 5.4, thus suggest that the wastewater is highly toxic and therefore not fit to be released into the environment. The toxicity of local dyeing wastewater to *D. magna* could be linked to high level of Zn, Fe, COD, TOC and TDS (see Table 2). These findings support previous work [1]. On the contrary, it was observed that *D. magna* toxicity decreased after photocatalytic treatment with the following nanomaterials: WO_3 (1.1), B/WO_3 (0.8), Al/WO_3 (0.4) and Al-B-WO_3 (0.2) respectively. Based on hazard classification system for wastewaters discharged into the aquatic environment, it can be concluded that wastewater treated with WO_3 alone with TU value of 1.1 has acute toxicity while that treated with B/WO_3 with TU (0.8) exhibits slight acute toxicity. It was found that toxicity unit (TU) value of local dyeing wastewater treated using Al/WO_3 and $Al/B/WO_3$ show no evidence of acute toxicity because TU value was less than 0.4 [56]. Similar trend was reported by Kim et al. [57] who reported toxicity reduction using electrocoagulation-electroflotation processes. The differences in the behavior of the nanocatalysts may be linked to their surface area and band gap energy. The daphnia toxicity test showed that treated wastewater had little or almost no toxicity depending on the nanocatalysts after 48 h whereas the raw wastewaters did.

3.5. Stability and reusability of nanocatalysts

Cost reduction has been reported as major attribute for the prevention and treatment of pollution due to solid waste at the industrial level [60]. Sequel to that, the photocatalytic regeneration capacity of undoped WO_3, B/WO_3, Al/WO_3 and Al/B doped WO_3 for dyeing wastewater treatment was investigated and the result shown in Fig. 18. Accordingly, the photocatalytic activity for dyeing wastewater by undoped WO_3, B/WO_3, Al/WO_3 and Al/B doped WO_3 were nearly 100% in the 1st, 2nd and third cycles. Beyond the third regeneration cycle, regeneration ability was observed to be above 85% even after 5th regeneration cycle. As observed, the photocatalytic activity of the nanoparticles was undoped WO_3 (85%), B/WO_3 (88%), Al/WO_3 (90%) and $Al/B/WO_3$ (93%) even after the 5th cycle. Considering cost reduction and the environmental protection, undoped WO_3, B doped WO_3, Al doped WO_3 and Al/B doped WO_3 showed reliable reusable attribute for photocatalytic degradation of dyeing wastewater. From Figs. 19 and 20, it could be seen that the mineralogical phase and morphology of the nanocatalysts after the 5th cycle was not completely destroyed, the slight changes may be occupation of the binding sites by the light and heavy pollutants, thus making their core-shell structures slightly distorted.

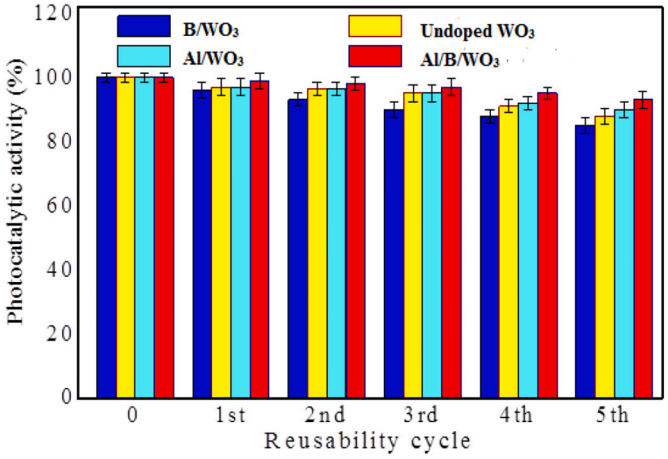

Fig. 18. Reusability assessment of undoped WO_3, B/WO_3, Al/WO_3 and $Al/B/WO_3$ for dyeing wastewater treatment.

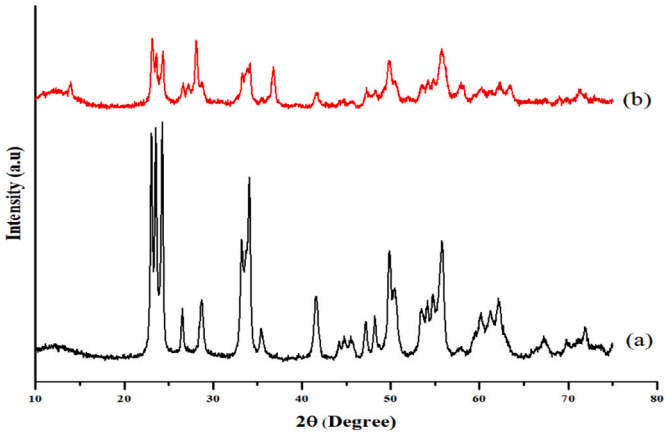

Fig. 19. XRD patterns of $Al/B/WO_3$ of (a) before (b) after recycling.

4. Conclusion

In summary, separate and simultaneous immobilization of WO_3 with Al and B were reported. The synthesized nanomaterials were examined using several characterization tools. The photocatalytic activity of the various prepared nanocatalysts over local dyeing wastewater under natural sunlight irradiation was investigated. The acute toxicity of untreated and treated wastewater was tested using *D. magna*. Based on these, the following conclusions were drawn. Addition of B and Al onto WO_3 did not distort its monoclinic phase but was responsible for the reduction of band gap energy from 2.42 eV (WO_3) to 1.70 eV (Al/B doped WO_3).

Al/B doped WO_3 composite exhibited enhanced photodegradation efficiency better than its ordinary WO_3, B/WO_3 and Al/WO_3 with total organic carbon (TOC) and chemical oxygen demand (COD) reduction efficiency of 96.5% and 97.3% due to differences in band gap and specific surface area. Bare WO_3 performed better under natural sunlight irradiation than B doped WO_3 due to the presence of carbon doping effect in the former than the latter. The kinetic data demonstrated that the photodegradation of the dye molecules in local dyeing wastewater by Al/B doped WO_3 nanocomposites was faster than the monodoped WO_3 and bare WO_3 nanoparticles and the experimental kinetic data obeyed the pseudo-first order followed by modified Freundlich and pseudo-second order model. This study demonstrated that $Al/B/WO_3$ nanocomposites could be reusable even after five cycles while *Daphnia* toxicity test showed that treated wastewater had little or almost no

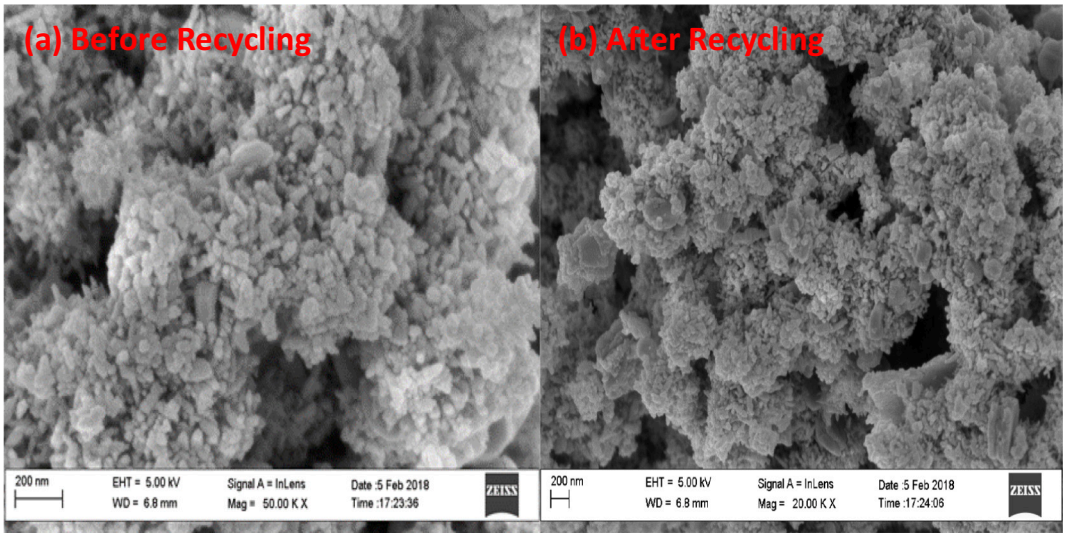

Fig. 20. HRSEM micrograph of Al/B/WO_3 of (a) before (b) after recycling.

toxicity depending on the nanocatalysts after 48 h whereas the raw wastewaters did. The toxic nature of the raw wastewater may be due to its complex mixture, different physicochemical properties such as pH, turbidity as well as different organic and inorganic pollutants.

Declaration of competing interest

The authors declared no conflict of interest.

Acknowledgements

The authors acknowledged Tertiary Education Trust Fund, Nigeria, with grant number (TETFUND/FUTMINNA/2016-2017/6th BRP/11) for the sponsorship. The authors appreciate the contribution of the following people for their technical assistance: Dr. Remy Bucher (XRD analysis, iThemba Labs, South Africa); Dr. Franscious Cummings (HRSEM/HRTEM/SAED/EDS) analysis, Physics department, University of the Western Cape (UWC), South Africa); and Prof. W.D. Roos for XPS analysis.

References

[1] J. Na, Y. Yoo, G. Nam, J. Jung, Effect of low-purity Fenton reagents on toxicity of textile dyeing effluent to *Daphnia magna*, Environ. Sci. Process. Imp. (2017), https://doi.org/10.1039/c7em00078b.
[2] A.M. Castro, V. Nogueira, I. Lopes, T. Rocha-Santos, R. Pereira, Evaluation of the potential toxicity of effluents from the textile industry before and after treatment, Appl. Sci. 9 (2019) 3804.
[3] Y. Yu, B. Wu, L. Jiang, X.X. Zhang, H.Q. Ren, M. Li, Comparative analysis of toxicity reduction of wastewater in twelve industrial park wastewater treatment plants based on battery of toxicity assays, Sci. Rep. 9 (2019) 3751.
[4] R.D. Kale, P. Kane, Colour removal using nanoparticles, J. Text. Technol. 1 (1) (2015) 23–32.
[5] E. Liwarska-Bizukojc, R. Ślęzak, M. Klink, Study on wastewater toxicity using ToxTrak™ method, Environ. Sci. Pollution Res. 23 (2016) 9105–9113.
[6] E.P. Thiyagarajan, P.S. Sargvanan, N.N. Devi, S. Gandlic, D. Renganathan, Bisorption of reactive red using positively charged metapenaeusmonoceros shell, J. Saudi Chem. Soc. 15 (4) (2013) 62–75.
[7] S. Khan, A. Malik, Environmental and health effects of textile industry wastewater, Manchester metropolitan Uni, J. Environ. Sci. 14 (6) (2013) 567–575.
[8] C.A. Bode-Aluko, O. Pereao, H.H. Kyaw, L. Al-Naamani, M.Z. Al-Abri, M.T. Z. Myint, A. Rossouw, O. Fatoba, L. Petrik, S. Dobretsov, Photocatalytic and antifouling properties of electrospun TiO_2 polyacrylonitrile composite nanofibers under visible light, Mater. Sci. Eng. B 264 (2021), 114913.
[9] A. Fakhri, S. Behrouz, Photocatalytic properties of tungsten trioxide (WO_3) nanoparticles for degradation of Lidocaine under visible and sunlight irradiation, Sol. Energy 112 (2015) 163–168.
[10] A. Nedal, V. Marei, Textile Wastewater Treatment by Magnetic Nanoadsorbent. Project: Nanotechnology for Textile Wastewater Treatment, AnNajah University, Nablus Press, Palestine, 2013, pp. 32–35.
[[11] N. Rohmah, D. Roosmini, M.A. Septiono, Study of whole effluent acute toxicity test (*Daphnia magna*) as an evaluation of Ministry of Environment and Forestry Decree No. 3 in 2014 concerning industrial performance rank in environmental management, in: MATEC Web of Conf vol. 147, 2018, p. 08005.
[12] F. Gholami-Borujeni, F. Nejatzadeh-Barandozi, H. Aghdasi, Data on effluent toxicity and physicochemical parameters of municipal wastewater treatment plant using *Daphnia magna*, Data Brief 19 (2018) 1837–1843.
[13] S. Khan, M. Anas, A. Malik, Mutagenicity and genotoxicity evaluation of textile industry wastewater using bacterial and plant bioassays, Toxicol. Rep. 6 (2019) 193–201.
[14] A. Hasani, Q.V. Le, T.P. Nguyen, K.S. Choi, W. Sohn, J.K. Kim, H.W. Jang, S.Y. Kim, Facile solution synthesis of tungsten trioxide doped with nanocrystalline molybdenum trioxide for electrochromic devices, Sci. Rep. 7 (2017) 13258.
[15] H. Lee, M. Kim, D. Sohn, S.H. Kim, S.G. Oh, S.S. Im, I.S. Kim, Electrospun tungsten trioxide nanofibers decorated with palladium oxide nanoparticles exhibiting enhanced photocatalytic activity, R. Soc. Chem. Adv. 7 (2017) 6108.
[16] M. Arshad, M. Ehtisham-ul-Haque, M. Bilal, N. Ahmad, A. Ahmad, M. Abbas, J. Nisar, M.I. Khan, A. Nazir, A. Ghaffar, M. Iqbal, Synthesis and characterization of Zn doped WO_3 nanoparticles: photocatalytic, antifungal and antibacterial activities evaluation, Mater. Res. Express 7 (2020), 015407.
[17] S. Chen, Y. Xiao, W. Xie, Y. Wang, Z. Hu, W. Zhang, H. Zhao, Facile strategy for synthesizing non-stoichiometric monoclinic structured tungsten trioxide (WO_{3-x}) with plasma resonance absorption and enhanced photocatalytic activity, Nanomaterials 8 (2018) 553.
[18] J. Sun, B. Li, Q. Wang, P. Zhang, Y. Zhang, L. Gao, X. Li, Preparation of phosphorus-doped tungsten trioxide nanomaterials and their photocatalytic performances, Environ. Technol. (2020), https://doi.org/10.1080/09593330.2020.1745292.
[19] A. Abdrashid, B.C. Daniel, N.H. Saad, M.A. Maisara, Hydrothermal synthesis of tungsten trioxide nano structure using sodium chloride as directing agent, J. Multidiscip. Eng. Sci. Technol. 2 (6) (2015) 1572–1576.
[20] S.M. Harshulkhan, K. Janaki, G. Velraj, R.S. Ganapthy, M. Nagarasam, Synthesize of silver doped tungsten oxide nanoparticle and its photocatalytic activity, J. Mater. Sci. 16 (27) (2016) 4744–4751.
[21] N. Prabhu, S. Agilan, A. Muthuxum, Thermal investigations of aluminium doped tungsten oxide nanoparticles by solvothermal cum chemical method, J. Ovon. Res. 5 (1) (2014) 34.
[22] V. Yadav, P. Verma, H. Sharma, S. Tripathy, V.K. Saini, Photodegradation of 4-nitrophenol over B-doped TiO_2 nanostructure: effect of dopant concentration, kinetics, and mechanism, environ, Sci. Pollut. Res. (2020), https://doi.org/10.1007/s11356-019-06674-x.
[23] D. Zappa, The influence of Nb on the synthesis of WO_3 nanowires and the effects on hydrogen sensing performance, Sensors 19 (2019) 2332.
[24] C.M. Wu, S. Naseem, M.H. Chou, J.H. Wang, Y.Q. Jian, Recent advances in tungsten-oxide-based materials and their applications, Front. Mater. 6 (2019) 49.
[25] M.M. Thwala, L.N. Dlamini, Photocatalytic reduction of Cr(VI) using Mg-doped WO_3 nanoparticles, Environ. Technol. (2019), https://doi.org/10.1080/09593330.2019.1629635.
[26] S. Wang T. Cochel, A. Manthiram, Synthesize of boron-doped carbon nanotube-supported by platinum nanoparticle, J. Phys. Chem. R. Soc. Chem. 12 (7) (2012) 24–32.
[27] P. Niu, G. Wu, P. Chen, H. Zheng, Q. Cao, H. Jiang, Optimization of boron doped TiO_2 as an efficient visible light-driven photocatalyst for organic dye degradation with high reusability, Front. Chem. 8 (2020) 172.
[28] S. Hassan, A review on nanoparticles: their synthesis and types, Res. J. Recent Sci. 4 (2) (2015) 9–11.
[29] E.K. Heidari, S.R. Mahmoodi, M.B. Ehsan, Synthesis and manipulation of tungsten oxide nanoparticles for gas sensing applications, Int. J. Phys. 5 (1) (2012) 227–233.

[30] T.T. Nguyen, S.N. Nam, J. Son, J. Oh, Tungsten trioxide (WO_3)-assisted photocatalytic degradation of amoxicillin by simulated solar irradiation, Sci. Rep. 9 (2019) 9349.
[31] J.O. Tijani, O. Ugochukwu, L.A. Fadipe, M.T. Bankole, A.S. Abdulkareem, W. D. Roos, One-step green synthesis of WO_3 nanoparticles using *Spondias mombin* aqueous extract: effect of solution pH and calcinations temperature, Appl. Phys. A 125 (2019) 162.
[32] S. Baker, S. Satish, Endophytes: toward a vision in synthesis for future therapeutic agent, Int. J. Bio-inorg. Hybrid. Nanopart. 1 (5) (2013) 11–12.
[33] W. Chu, Y.F. Rao, Photocatalytic oxidation of monuron in the suspension of WO_3 under the irradiation of UV–visible light, Chemosphere 86 (11) (2011) 1079–1086.
[34] D. Sánchez Martínez, A. Martínez-de la Cruz, E. López Cuéllar, Photocatalytic properties of WO_3 nanoparticles obtained by precipitation in presence of urea as complexing agent, Appl. Catal. A Gen. 398 (2011) 179–186.
[35] Y. Wicaksana, S. Liu, J. Scolt, R. Amal, Tungsten trioxide as a visible light photocatalyst for volatile organic carbon removal, Molecules 19 (1) (2014) 1747–1762.
[36] H. Widiyandari, I. Firdaus, V.G.S. Kadarisman, A. Purwanto, Optical properties and photocatalytic activities of tungsten oxide (WO_3) with platinum co-catalyst addition, AIP Conf. Proc. 1712 (2016), 050027.
[37] J.O. Tijani, O. Ugochukwu, L.A. Fadipe, M.T. Bankole, A.S. Abdulkareem, W. D. Roos, Photocatalytic degradation of local dyeing wastewater by iodine-phosphorus co-doped tungsten trioxide nanocomposites under natural sunlight irradiation, J. Environ. Manag. 236 (2019) 519–533.
[38] J.O. Tijani, U.O. Momoh, R.B. Salau, M.T. Bankole, A.S. Abdulkareem, W.D. Roos, Synthesis and characterization of $Ag_2O/B_2O_3/TiO_2$ ternary nanocomposites for photocatalytic mineralization of local dyeing wastewater under artificial and natural sunlight irradiation, Environ. Sci. Pollut. Res. 26 (19) (2019) 19942–19967.
[39] APHA, Standard Methods for Examination of Water and Wastewater, 20th ed., American Public Health Association, Washington, DC, 1998.
[40] MOE Korea, Standard Methods for Examination of Water Quality, Ministry of Environment, Sejong, Republic of Korea, 2014.
[41] L. Ghasemi, H. Jafari, Morphological characterization of tungsten trioxide nanopowder synthesised by sol-gel modified pechini method, J. Mater. Sci. 20 (6) (2017) 1713–1721.
[42] J. Zhang, K. Tse, M. Wong, Y. Zhang, Y. Zhu, Mechanism of doping nanomaterial, J. Front. Phys. 11 (2) (2016) 23–28.
[43] N. Prabhu, S. Agilan, N. Muthukumarasamy, Effect of temperature on aluminum doped WO_3 nanoparticles prepared by solvo thermal method. Optoelectron. Adv. Mater. Rapid Commun. 9 (3–4) (2015) 394–397.
[44] E.L. Hipolito, A.M. Lacruz, Q.L. Yu, H.J.H. Brouwers, Precipitation synthesis of WO_3 for NO_X removal using PEG as template, Ceram. Inter. J. 40 (14) (2014) 12128.
[45] N.K. Hang, N.A. Jaffar, L.L. Minggu, M.B. Kassim, Fabrication and characterization of Fe-doped tungsten trioxide photoelectrode in aqueous medium using tungstic acid and ferrocene as starting materials, Malay. J. Anal. Sci. 20 (4) (2016) 923–930.
[46] W. Li, J. Li, X. Wang, Q. Chen, Preparation and water-splitting photocatalytic behavior of S-doped WO_3, Appl. Surf. Sci. 263 (2012) 157–162.
[47] W. Mu, X. Xie, X. Li, R. Zhang, Q. Yu, K. Lv, H. Wei, Y. Jian, Characterizations of Nb-doped WO_3 nanomaterials and their enhanced photocatalytic performance, R. Soc. Chem. Adv. 4 (2014) 36064–36070.
[48] X. Hu, P. Xu, H. Gong, G. Yin, Synthesis and characterization of WO_3/graphene nanocomposites for enhanced photocatalysts activities by one-step in situ hydrothermal reaction, Int. J. Mater. Sci. 11 (2) (2018) 142–154.
[49] G.R. Bamwenda, H. Arakawa, The visible light induced photocatalytic activity of tungsten trioxide powders, Appl. Catal. A Gen. 210 (2001) 181–191.
[50] World Health Organization, Safely Managed Drinking Water: Thematic Report on Drinking Water 2017, 2017.
[51] D. Bhatia, N.R. Sharma, R. Kanwar, J. Singh, Physicochemical assessment of industrial textile effluents of Punjab (India), Appl Water Sci 8 (2018) 83.
[52] O.E. Odipe, R.M. Olalekan, F. Suleiman, Assessment of heavy metals in effluent water discharges from textile industry and river water at close proximity: a comparison of two textile industries from Funtua and Zaria, North Western Nigeria, Madridge, J. Agric. Environ. Sci. 1 (1) (2019), 1000101.
[53] S. Reddy, W.J. Osborne, Heavy metal determination and aquatic toxicity evaluation of textile dyes and effluents using *Artemia salina*, Biocatal. Agric. Biotechnol. 25 (2020), 101574.
[54] M.D.N. Ramos, J.P.P. Lima, S.F. de Aquino, A. Aguiar, (2021). A critical analysis of the alternative treatments applied to effluents from Brazilian textile industries. J. Water Process Eng. 43 (2021) 102273.
[55] L. Wang, W. Du, Z. Hu, K. Uvdal, L. Li, W. Huang, Hybrid rhodamine fluorophores in the visible–NIR region for biological imaging, J. Germ. Chem. Soc. 58 (40) (2019) 14026–14043.
[56] E.M. Ngigi, P.N. Nomngongo, J.C. Ngila, Synthesis and application of Fe-doped WO_3 nanoparticles for photocatalytic degradation of methylparaben using visible–light radiation and H_2O_2, Catal. Lett. 149 (1) (2019) 40–60.
[57] H.L. Kim, J.B. Cho, Y.J. Park, I.H. Cho, Treatment and toxicity reduction of textile dyeing wastewater using the electrocoagulation-electroflotation process, J. Environ. Sci. Health A 51 (8) (2016) 661–668.
[58] H. Liu, T. Peng, D. Ke, Z. Peng, C. Yan, Preparation and photocatalytic activity of dysprosium doped tungsten trioxide nanoparticles, Mater. Chem. Phys. (104) (2007) 377–383.
[59] I. Vamvasakis, I. Georgaki, D. Vernardou, G. Kenanakin, N. Katsarakis, Synthesis of WO_3 catalytic powders: evaluation of photocatalytic activity under NUV/visible light irradiation alkaline reaction, J. Sol-Gel Sci. Technol. 15 (5) (2015) 1–9.
[60] T.C. Egbosiuba, A.S. Abdulkareem, J.O. Tijani, J.I. Ani, V. Krikstolaityte, M. Srinivasan, A. Veksha, G. Lisak, Taguchi optimization design of diameter-controlled synthesis of multi walled carbon nanotubes for the adsorption of Pb(II) and Ni(II) from chemical industry wastewater, Chemosphere 266 (2021) 128937.
[61] R Banala R, V Nagati B, P Karnati R, Green synthesis and characterization of Carica papaya leaf extract coated silver nanoparticles through X-ray diffraction, electron microscopy and evaluation of bactericidal properties, Saudi J. Biol. Sci. 22 (5) (2015) 637–644.